

Joint Focal Mechanism Inversion Using Downhole and Surface Monitoring at the Decatur, Illinois, CO₂ Injection Site

Nadège Langet^{*1}, Bettina Goertz-Allmann¹, Volker Oye¹, Robert A. Bauer², Sherilyn Williams-Stroud², Anna Maria Dichiariante¹, and Sallie E. Greenberg²

ABSTRACT

The three-year CO₂ injection period at the Illinois Basin - Decatur Project site (Decatur, Illinois, United States) produced a number of microseismic events distributed in very distinct spatiotemporal clusters with different orientations. Further characterization of the microseismicity encompasses the determination of the event source mechanisms. Initially, the microseismic monitoring network consisted solely of borehole sensors, but has been extended with surface sensors, thereby significantly improving the data coverage over the focal sphere. This article focuses on 23 events from the northernmost microseismic cluster (about 2 km from the injection point) and takes advantage of both, surface and downhole, recordings. The resulting strike-slip east–west-oriented focal planes are all consistent with the east–west orientation of the cluster in map view. The injection-related increase of pore pressure is far below the formation fracture pressure; however, small stress-field changes associated with the pore-pressure increase may reach as far as to the investigated cluster location. Monte Carlo modeling of the slip reactivation potential within this cluster showed that the observed maximum stress-field orientation of N068° is the optimum orientation for fault reactivation of the east–west-oriented cluster. Our results suggest that the east–west orientation of the investigated cluster is the main reason for its activation, even though the cluster is about 2 km away from the low-pressure injection point.

KEY POINTS

- We want to better understand the causes of induced seismicity in the case of a CO₂ injection.
- Fault reactivation is likely one of the main causes of microseismicity, at least for the investigated cluster.
- Fault reactivation is not the only process at play and analyses have to be carried out at the other clusters.

Supplemental Material

(van der Baan *et al.*, 2013), geothermal energy (Zang *et al.*, 2014), and also carbon storage (Will, El-Kaseeh, *et al.*, 2016). This tool can inform the extent to which pore pressure and other stress changes affect deformation within a reservoir (e.g., Albaric *et al.*, 2013). Although differences in geological and geophysical initial conditions tend to have an impact on the mechanisms involved in the generation of microseismicity, the common understanding is that induced seismicity can result from two main processes: pore-pressure variations due to the fluid propagation or from stress redistribution and transfer. In addition, the geology as well as other processes such as thermal and geochemical are at play and add even more complexity (Vilarasa *et al.*, 2019).

INTRODUCTION AND CONTEXT

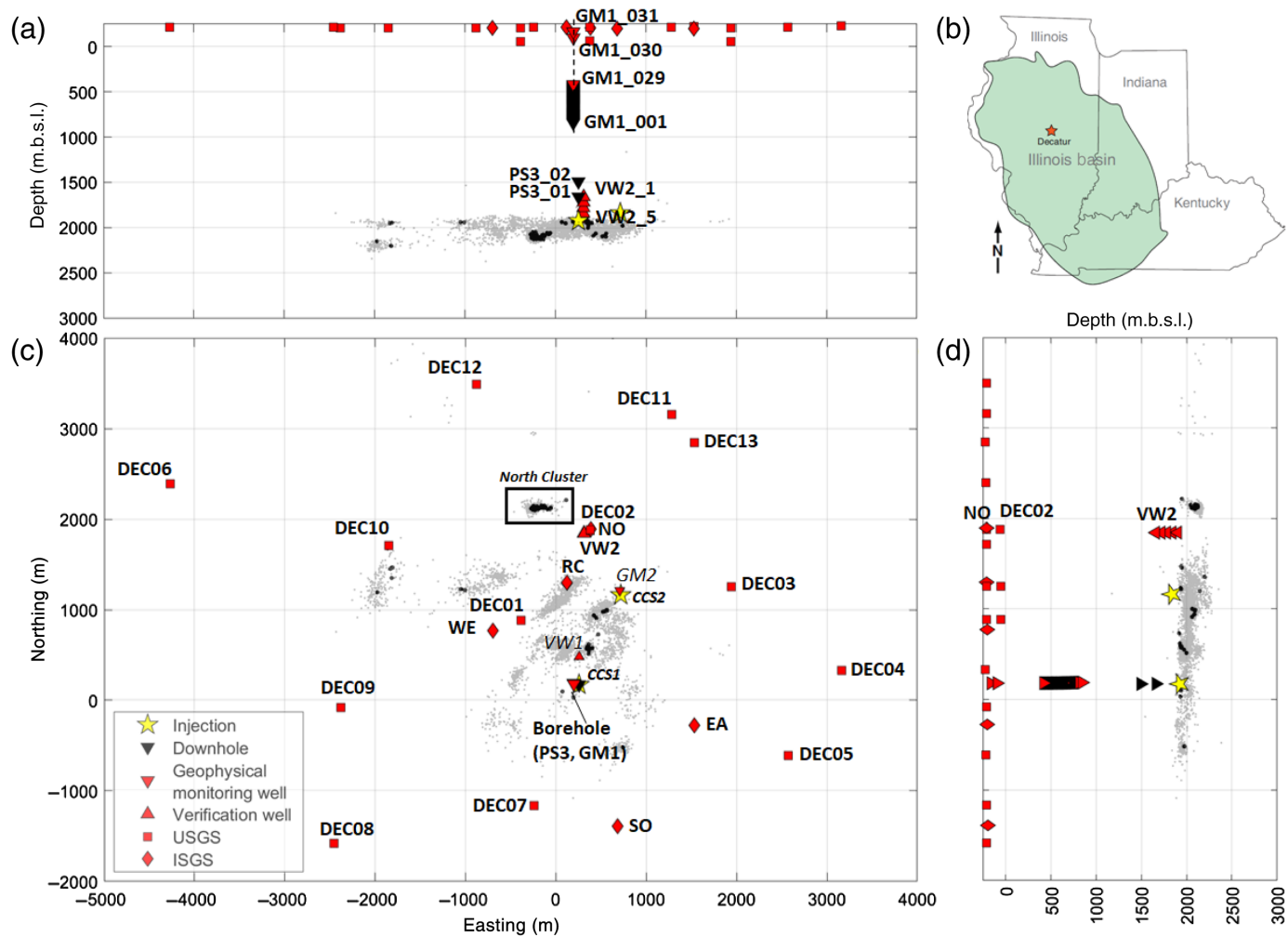
During the last decade, carbon dioxide (CO₂) storage has become an important environmental topic to reduce CO₂ emissions into the atmosphere. Several sites worldwide have already been developed and used for carbon storage (e.g., Oye *et al.*, 2013; Furre *et al.*, 2017; Rock *et al.*, 2017). However, there is still a need for better understanding of the effect of CO₂ injection at depth. In the recent years, microseismic monitoring has been extensively used as a diagnostic tool in many applications such as shale gas hydraulic fracturing

1. NORSAR, Kjeller, Norway; 2. Illinois State Geological Survey, University of Illinois at Urbana-Champaign, Champaign, Illinois, U.S.A.

*Corresponding author: nadège@norsar.no

Cite this article as: Langet, N., B. Goertz-Allmann, V. Oye, R. A. Bauer, S. Williams-Stroud, A. M. Dichiariante, and S. E. Greenberg (2020). Joint Focal Mechanism Inversion Using Downhole and Surface Monitoring at the Decatur, Illinois, CO₂ Injection Site, *Bull. Seismol. Soc. Am.* **110**, 2168–2187, doi: [10.1785/0120200075](https://doi.org/10.1785/0120200075)

© Seismological Society of America



The Illinois Basin - Decatur Project (IBDP) is the first Bioenergy Carbon Capture and Storage project in the United States that injected a large volume of supercritical CO₂ into an undisturbed saline formation (Finley *et al.*, 2013). The injection phase of the project ran over a 3 yr period (from November 2011 to November 2014) during which one million cubic meters of CO₂ were injected in the CCS1 well (Fig. 1c) into the Lower Mount Simon Sandstone Formation, close to the Precambrian basement, at about 2 km depth. A second injection, from a new injector (CCS2) about 1 km northeast of CCS1, into the same reservoir formation but at a shallower depth, started in September 2017 within the framework of the Illinois Industrial CCS Sources project (which is not discussed in this article). More details about the projects and facilities are given in S. Williams-Stroud *et al.* (unpublished manuscript, 2020; see Data and Resources).

The Illinois basin (Fig. 1b) is an intracratonic basin that lies within the east-northeast–west-southwest compressive stress field of the North American plate (Lahann *et al.*, 2017). The Precambrian basement at IBDP is composed of unmetamorphosed rhyolite and can be highly fractured, the fractures potentially being filled with clay. At IBDP, the reservoir

Figure 1. (a,d) Cross sections and (c) map view of the Illinois Basin - Decatur Project (IBDP) site showing the seismic network and the overall seismicity (gray dots) detected and located with the downhole sensors (GM1, PS3, and VW2). Black filled dots correspond to events that were also clearly visible on the U.S. Geological Survey (USGS) surface stations (DEC) and Illinois State Geological Survey (ISGS) surface stations. Stars represent the injection wells. In this article, we particularly focus on 23 events belonging to the north cluster (black rectangle in map view). Seismic station names are indicated in bold; other geophysical and verification wells without seismic instrumentation are in italic. (b) Map of the midwest region of the United States. The shaded area represents the Illinois basin, and the star shows the location of the IBDP site (from Freiburg *et al.*, 2014). m.b.s.l., meters below sea level; N, north. The color version of this figure is available only in the electronic edition.

formation is the Lower Mount Simon unit composed of sandstones of miscellaneous origins (such as e.g., fluvial and marine, Freiburg *et al.*, 2014). The observed heterogeneities confer different properties to the reservoir formation, from high quality for the Lower Mount Simon (i.e., high permeability and porosity) to low quality for the Middle and Upper Mount Simon due to the alternance of mudstones and sandstones. These heterogeneities should also confine the fluid flow

in horizontal directions. The lowest portion of the Mount Simon Sandstone overlying the basement is the informally named Argenta Formation. At CCS1, it is less than 15 m thick and composed of fine- to medium-grain size sandstone of low porosity (<10%) and low permeability (<36 mD) (Freiburg *et al.*, 2014). The reservoir formation is overlain and sealed by impermeable shale formations (Eau Claire, Maquoketa, and New Albany).

A first verification well (VW1) was drilled about 300 m away from the injection well down to about 2000 m depth, where pore pressure and other hydraulic parameters were measured, and a first geophysical monitoring well (GM1) was instrumented nearby the injection (see Fig. 1). Later on, a second verification well (VW2) and a second geophysical monitoring well (GM2) were drilled. Permanent seismic monitoring has been a part of the project from before injection with the installation of borehole sensors in some of the aforementioned monitoring wells (Will, Smith, *et al.*, 2016), followed by the installation of surface sensors in the course of 2013 both by the U.S. Geological Survey (USGS) and the Illinois State Geological Survey (ISGS).

A detailed analysis of the microseismicity has been carried out (Couëslan *et al.*, 2014; Bauer *et al.*, 2016; Will, Smith, *et al.*, 2016; Goertz-Allmann *et al.*, 2017). Nearly 20,000 potential microseismic events were detected by the downhole sensors during the 3 yr injection period plus postinjection to date. Approximately 25% of the detected events could be located with certainty at multiple borehole arrays, and moment magnitudes were estimated (Will *et al.*, 2014). Most events have negative moment magnitudes and are located in distinct spatial clusters (Fig. 1) with a dominant northeast–southwest orientation in map view, which is consistent with optimally oriented failure planes for the maximum horizontal stress direction of 68° (Bauer *et al.*, 2016). This suggests reactivation of pre-existing faults (Lee *et al.*, 2014; Bauer *et al.*, 2016), although no such faults were identified on earlier interpretations of seismic profiles (Finley *et al.*, 2013). Goertz-Allmann *et al.* (2017) analyzed two of the clusters more thoroughly and observed a spatiotemporal migration of the seismicity from the reservoir into the basement, reinforcing the hypothesis of the existence of basement faults extending up into the lower part of the reservoir formulated by Couëslan *et al.* (2014) and Kaven *et al.* (2015) and supported by outcrop studies and well logs in comparable geological formations (Mulvany and Thompson, 2013). However, the orientation of the different clusters shows some variability, and also the distance to the injection varies. As such, the processes that steer the occurrence and characteristics of the seismicity clusters likely differ and contain complexity. To unravel the different processes at work, we here determine focal mechanisms as a complement to event location.

In the next section, we first recall what information is necessary for determining a source mechanism, as well as the

approach used in this article. We will then describe in more details the data.

PREREQUISITES AND PRACTICAL APPROACH FOR DETERMINING SOURCE MECHANISMS

Many methods exist to determine seismic event source mechanisms, from simple to more complex, such as, for example, moment tensor inversion from full waveforms (Jost and Herrmann, 1989; Julian *et al.*, 1998). Here, we chose a relatively simple approach, which consists in measuring the *P*-wave first-motion polarities and compare them with the sign of the theoretical radiation pattern coefficients using the formula developed by Ou (2008) for tensile faults. There are two reasons for our choice: (1) working solely with polarities does not require knowledge of the medium attenuation or of anything else that could affect the amplitudes and (2) *P* waves are usually easier to identify than any other phases in the seismograms: they are the first waves recorded, and they (in principle) cannot be mistaken, in contrast to *S* waves, which are more readily confused with converted waves (here the polarity of such waves may change) and/or be hidden in the coda waves generated by scattering on the heterogeneities. Kaven *et al.* (2015) computed focal mechanisms of a selected number of events of the USGS catalog using the *P*-wave first-motion polarities from only the USGS surface stations as input into the HASH program (Hardebeck and Shearer, 2002). We will directly compare their mechanisms with our study's results, which include more surface sensors and important downhole data.

Apart from polarities, we also need to know the event location to be able to compute ray angles (direction of propagation from north—azimuth—and take-off angle at the source). The ray angle computation is strongly dependent on the event location, and both, ray angle and event location, require an accurate knowledge of the velocity model (Fig. 2). The ray angles define the distribution of the station network on the focal sphere and are thus of particular importance for determining the source mechanism and its reliability.

Ensuring that sensors are correctly oriented in the geographical coordinate system is also important, especially if horizontal components are used. We only used vertical components to pick *P*-wave polarities and found some inconsistencies for the two deeper sensors. After verification, their vertical component was flipped (more details in the supplemental material to this article).

The inversion itself is based on a grid search over the strike, dip, and rake angles, which describe a pure double-couple mechanism. Because of the inherent ambiguity between fault and auxiliary planes for a given solution and due to the symmetry properties of a sphere, the grid search can be reduced from 0° to 180° for the strike ϕ , 0° to 90° for the dip δ , and -90° to 90° for the rake λ . We use an increment of 5° for all angles, which is in agreement with the expected accuracy derived from the given network geometry (see next section)

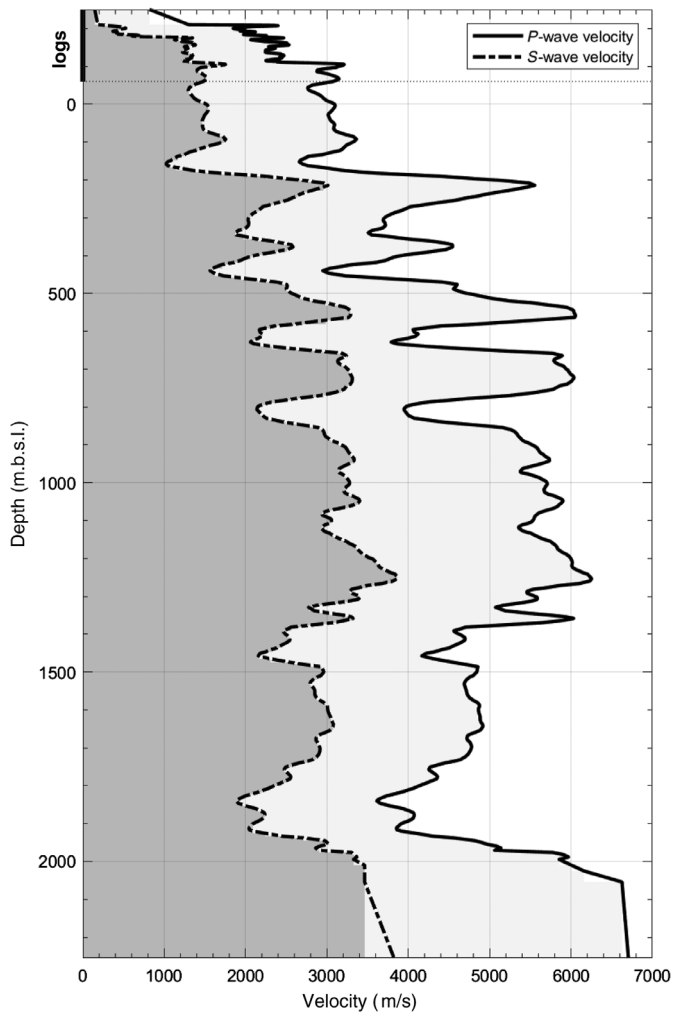


Figure 2. Velocity model used for event location and ray angles computation. Continuous line, P -wave velocities; dashed line, S -wave velocities. The zero level corresponds to mean sea level. Horizontal dotted lines represent the parts of the model that were modified and derived from available subsurface velocity logs.

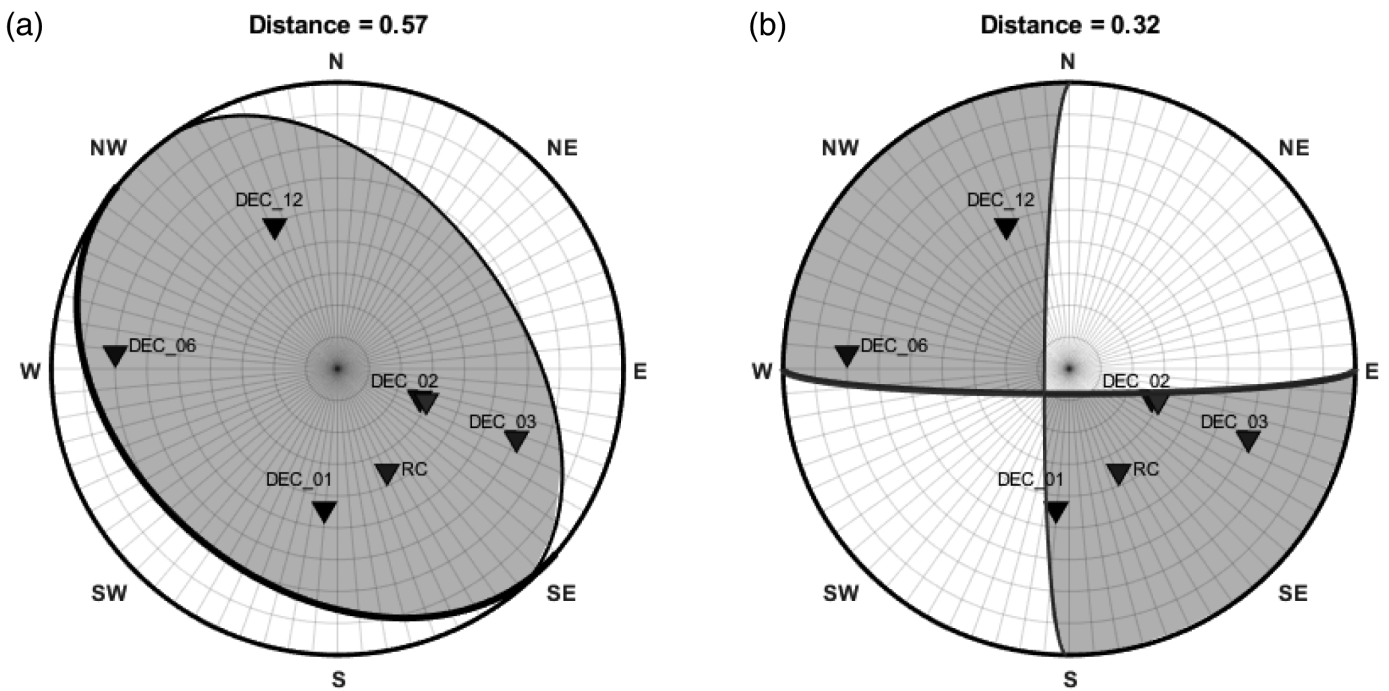
and in addition reduces computation time. The decision to neglect the tensile angle from the grid search was made after first tests showed rather small tensile components, lying within the uncertainty bounds of our solutions. Indeed, small tensile components do not necessarily depict a real behavior at the source, but are rather an artifact of the method: fitting a tensile mechanism rather than a double couple will always be easier, because one of our decision criteria to define the best solution is the distance to the nodal planes, which, in turn, depends on the network geometry. Hence, we constrained the focal mechanism to double-couple solutions by setting the tensile angle to 0° .

For each tested combination of angles, the theoretical P -wave radiation pattern coefficients are computed using the formula detailed in Ou (2008) and implemented in a MATLAB code by Kwiatek (2020). Because we use the polarities, only the sign of the coefficients turns out to be of interest. The theoretical

radiation pattern coefficients are different for each event and depend on the way the ray propagates from the source to each station (azimuth and take-off angles). Indeed, we can compare picked polarities with theoretical ones only after having projected the station network on one of the hemispheres of the focal sphere. We chose the lower hemisphere as a convention in this article. As mentioned earlier, the computation of the ray angles is dependent on event location and hence, to a greater extent, on medium velocity. For that purpose, ray paths are computed by solving the eikonal equation for a 1D velocity model, and the take-off angle is considered as the slope of the first five samples of the ray path measured clockwise with respect to the vertical axis pointing downward. In a later section, the sensitivity of ray angles to different velocity models and event locations will be tested and discussed.

Picked polarities, and theoretical polarities computed for a given network distribution over the focal sphere, are compared for different combinations of fault angles (ϕ, δ, λ). Each comparison consists of counting the number of polarity reversals between observations and predictions. A reversal is defined when the observed and predicted polarities are of opposite sign and is the parameter that should be minimized in priority. However, a given number of reversals may not result in a unique solution, but in a range of potential solutions. This is particularly true if the station coverage becomes sparse (only some areas of the focal sphere are well constrained), due to, for example, a low number of observations and/or inconsistent observations. To avoid having too many potential solutions among which it is difficult to choose, we introduce a secondary criterion to define the best solution, by measuring the distance to the nodal planes. The idea behind this is that the closer a station is to one of the nodal planes, the smaller the P -wave amplitude should be and hence the more ambiguous the P -wave polarity measured at that station may become. Or, on the contrary, the farther a station is from the nodal planes, the more trustworthy the measured polarity should be, as the radiated P -wave amplitude should be large. Consequently, two scenarios can be foreseen. (1) The correspondence between data and theory is perfect, that is, the number of polarity reversals is zero. In this case, we assume that the picked polarities can be trusted and decide that the best solution is the one that maximizes the distance of the projected stations to the nodal planes. (2) The correspondence between data and theory is not perfect, that is, there is at least one polarity reversal, and no existing mechanism could explain exactly our observations. Thus, we are less confident in our mismatched observations, but we still want to keep a higher confidence level for the observations that are well matched. In this case, we decide that the best solution is the one that minimizes the distance to the nodal planes of the stations, the observed polarities of which do not agree with the predicted ones.

In the inversion, the distance value is a weighted average of the distances of each individual station, with the weights



depending on the quality assigned to each polarity measurement. As our qualities range from A to E (see next section), we used weights of 0.35, 0.3, 0.25, 0.1, and 0, when the distance should be maximized (no polarity reversals, more weight is given to observations with higher confidence, which should be farther from the nodal planes) and 0.65, 0.7, 0.75, and 0.9, when the distance should be minimized (at least one polarity reversal, more weight is given to observations with lower confidence, which should be closer to the nodal planes). Let us define $N_{\text{reversals}}$ as the 3D matrix of $\text{length}(\phi) \times \text{length}(\delta) \times \text{length}(\lambda)$, in which ϕ , δ , and λ are the vectors containing all the possible values for the strike, dip, and rake angles, respectively. Let us find m , the minimum number of polarity reversals among all tested mechanisms: $m = \min(N_{\text{reversals}})$.

- If $m = 0$ and $\sum(N_{\text{reversals}} = m) > 1$, the best solution (ϕ, δ, λ) is the one whose distance = $\max\left(\frac{\sum_k(|\vec{n} \cdot \vec{p}_k| + |\vec{s} \cdot \vec{p}_k|) \times w_k}{2 \sum_k w_k}\right)$ in which k refers to stations with correct polarities;
- If $m > 0$ and $\sum(N_{\text{reversals}} = m) > 1$, the best solution (ϕ, δ, λ) is the one whose distance = $\min\left(\frac{\sum_l(|\vec{n} \cdot \vec{p}_l| + |\vec{s} \cdot \vec{p}_l|) \times (1-w_l)}{2 \sum_l (1-w_l)}\right)$ in which l refers to stations with wrong polarities with respect to theory.
- \vec{p}_k are unit vectors corresponding to the coordinates of station k projected onto the focal sphere.
- \vec{n} and \vec{s} are unit vectors defining the nodal planes, i.e. the normal and slip vectors, respectively.
- w_k is the weight assigned to the polarity measurement made at the k th station, in our case taking the values 0.35 for an A quality, 0.3 for B, 0.25 for C, and 0.1 for D (all E measurements having been removed prior to the inversion).

Figure 3. Test case of how the algorithm chooses the best-fitting mechanism. Polar projection of stations colored by their polarities (black triangles for positive, white triangles for negative). Note that here all polarities are positive and the station distribution is not optimum, resulting in a wide range of potential solutions. We show two potential mechanisms in (a, b) that could perfectly fit the data. Based on the mean distance of each station to the nodal planes, the mechanism in (a) is preferred to the mechanism in (b). E, east; NE, northeast; NW, northwest; S, south; SE, southeast; SW, southwest; W, west.

We illustrate the concept with a real example in Figure 3, in which both panels (a,b) present the same station distribution with only positive polarities. This example only shows surface sensors (data will be introduced in the next section) and is poorly constrained. However, the example is well suited to explain our above-derived weighting concept. We show two of the very different mechanisms that might fit the data, either a thrust-faulting mechanism in (a) or a strike-slip mechanism in (b). “A” quality was assigned to DEC01 and DEC12, “B” to DEC06, and “C” to the rest. In the case of (b), only stations DEC03 and RC are not close to the nodal planes, and to a lesser extent, DEC12 and DEC06. Stations DEC01 and DEC02, on the other hand, are almost on the nodal planes. This is not observed in the case of (a), in which all stations are at some distance from the nodal planes (and particularly the two “A” observations at DEC01 and DEC12), which explains why mechanism (a) is ultimately preferred to mechanism (b). The choice of the best mechanism could still remain somewhat arbitrary and needs to be examined or rated before being validated.

For that reason, we defined a number of quality factors on the source mechanisms obtained from the inversion, with the goal of reflecting our level of confidence in them (lower for small values, higher for high values). Finding a proper quality factor remains quite subjective, and several definitions were used here, such as the number of polarity reversals ($N_{\text{reversals}}$, i.e., the number of wrongly picked polarities in comparison with the best-found solution) with respect to the number of measurements (N_{obs} , i.e., the number of polarities which were picked in total) normalized by the maximum number of polarities that could have been used in the inversion (MAX_{obs}): $Q_1 = \frac{N_{\text{obs}} - N_{\text{reversals}}}{\text{MAX}_{\text{obs}}}$.

MAX_{obs} is the same number for all events. The number of potential solutions (N_{sol}) corresponding to the minimum number of polarity reversals is also a good indicator by giving an idea of the stability of the solution and, hence, of its reliability: $Q_2 = Q_1 \times (1 - \frac{N_{\text{sol}} - \text{MIN}_{\text{sol}}}{\text{MAX}_{\text{sol}}})$.

To compare the analyzed events relatively with each other, we also assign a quality factor that is scaled by the minimum and maximum observed number of solutions across the whole dataset (i.e., events that have only a few potential solutions will be considered more reliable than events that have many potential solutions): $Q_3 = 1 - \frac{N_{\text{sol}} - \text{MIN}_{\text{sol}}}{\text{MAX}_{\text{sol}} - \text{MIN}_{\text{sol}}}$.

As shown in Figure 4, the event location affects the distribution of observations over the focal sphere. We also measure the azimuthal gap between stations included in the inversion and for which a polarity measurement was made: $Q_4 = 1 - \frac{\text{AzimuthalGap}}{180}$.

In the following sections, we describe the data, the workflow, and the verification that we made to get trustworthy source mechanism solutions.

DATA USED AND PRACTICAL APPROACH

Seismic monitoring has been performed at the Decatur site since the project was launched as early as May 2010 (i.e., before the first injection took place in November 2011) and initially consisted of two four-component sensors (PS3 1 and PS3 2) placed in the injection well, outside tubing, at respective depths of 1660 and 1492 m, and 31 three-component geophones (GM1-31) placed in a geophysical monitoring well approximately 60 m northwest from the injection well: 29 of them between 418 and 844 m depth and two closer to the surface. All depths are given with respect to mean sea level. Five three-component geophones were added in a second verification well VW2 in September 2013 (Will, Smith, et al., 2016). From July through October 2013, the USGS started additional continuous monitoring of the site by installing three stations in shallow boreholes (DEC01-03) and 10 stations at the surface (DEC04-13). All stations are composed of two three-component sensors (i.e., six channels): the surface stations combine both broadband seismometers and accelerometers, whereas the borehole stations combine accelerometers at the surface and geophones around 150 m below the surface. Later, four more

borehole stations (DEC14–DEC17) were added by the USGS. In addition, in 2013, the ISGS installed a network of five three-component seismometers in surface vaults. The list of stations included in this study is summarized in Table S1, and Figure 1 shows their geographical distribution.

In this study, the source mechanism analysis is carried out on a small subset of the events detected by the downhole sensors. The main reason for this choice is that we obtain the most reliable results when seismic events are observed from as many directions as possible. A sparse station distribution would result in an insufficient coverage on the focal sphere and would finally only provide a wide range of poorly constrained solutions. Hence, we focus on a cluster of events and a time period during which a maximum number of stations are in operation, including downhole and surface recordings, that is, USGS and ISGS stations, which were only deployed in the course of 2013. As surface data are generally noisier than downhole data, only data corresponding to some of the strongest events were retained for further analysis. For our purpose, we also need a significant number of observations at the surface networks with a good azimuthal distribution. In practice, we searched for common events based on a catalog of 150 events provided by the USGS for the area. About 134 events matched both the USGS and IBDP catalogs, and we kept 57 events that passed strict visual inspection. These events are highlighted in Figure 1 and belong to different clusters. Twenty-three events belong to the northern cluster (black box in Fig. 1). They range from 0 and 1 in magnitude and form the focus of this study. This northern cluster corresponds to the cluster A defined by Goertz-Allmann et al. (2017) and was identified as cluster 18 in Will, El-Kaseeh, et al. (2016), located farther from the injection point (about 2 km) and is not oriented in the north–east direction like the other clusters. Of the 23 analyzed events, the first one was recorded in July 2013 and the last one in February 2015.

The P -wave first-motion polarities for all selected events were picked manually on the vertical component of each station by two geophysicists, independently of each other. For noisy data at the surface and more generally to ensure a certain confidence on the picked polarities, the data were filtered in different frequency ranges on a visual basis, from low to high (e.g., 5–50, 15–100, and 20–150 Hz). The measurements were validated only if the polarity of the first wiggle remained consistent over these different filters (to avoid filtering effects). Borehole data usually did not require any filtering. An example of vertical-component records of a very good event is shown in Figure 5 for which data have been band-pass filtered in the frequency range 15–200 Hz. We then compared and merged the polarities picked by the respective geophysicists. The observations were near 100% agreement and most disparities were related to very noisy traces. Quality factors were assigned to each measurement, from “A” for very good estimates to “E” for poor estimates, and used as weights to help choosing

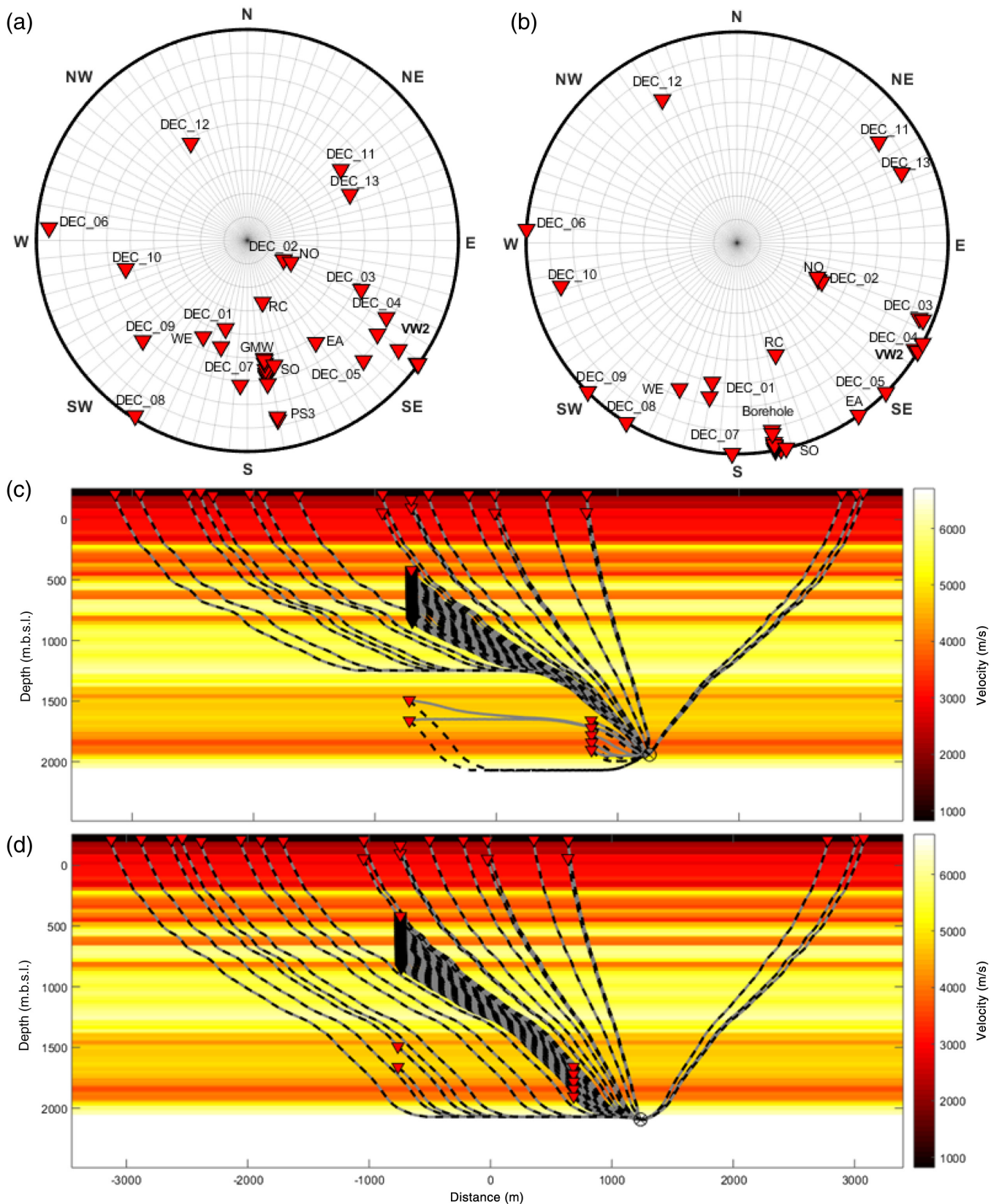


Figure 4. Influence of the depth of an event on the computation of ray paths and ray angles for the 1D velocity model. (a) Projection in polar coordinates of the station network on the focal sphere for the event location as shown in (c): shift of the cluster centroid by 200 m upward. (b) Same as (a) for the event location shown in (d): shift of the cluster centroid by 200 m

downward. (c,d) Ray paths corresponding to the first arrivals are dashed lines, whereas ray paths of the direct arrivals are continuous lines. The 1D velocity model is shown in the background with lighter colors for high velocities and darker colors for low velocities. The color version of this figure is available only in the electronic edition.

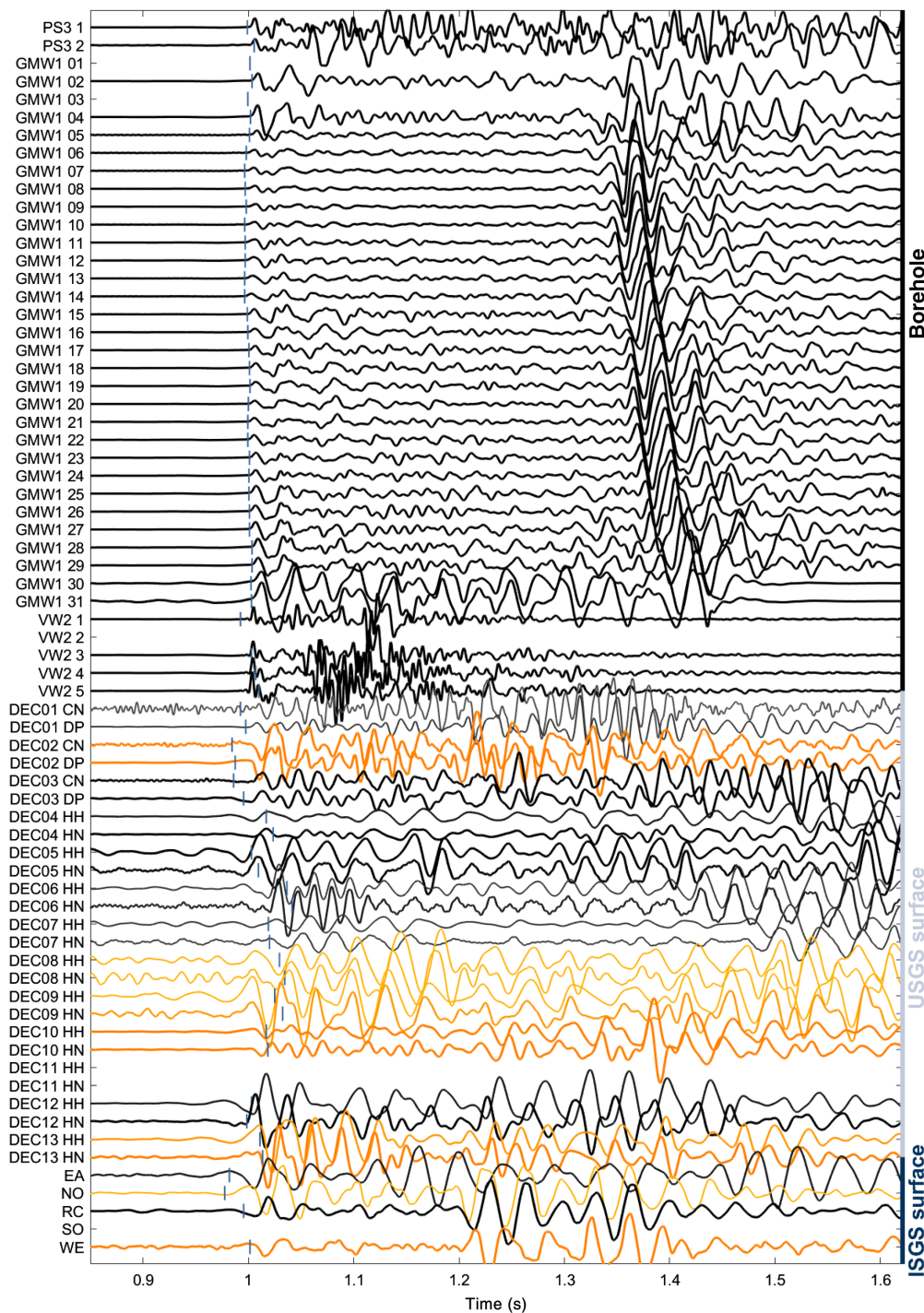


Figure 5. Waveforms (vertical component) of event 17 aligned on the first-phase arrivals. Amplitudes are not scaled and are artificially increased to make the first onset visible. Black traces show positive first-motion polarity; light-colored traces show negative first-motion polarity. Vertical bars represent the theoretical P -wave arrival times computed at the event location using the 1D velocity model. Polarities were in general defined as the sign of the first wiggle after the P wavepick. Suffixes for the USGS stations (DEC*) refer to accelerometers (HN), broadband seismometers (HH), shallow borehole (DP), and surface sensors (CN) (see Table S1). The color version of this figure is available only in the electronic edition.

the best mechanism during the inversion (as described in the previous section). In the end, we chose not to include measurements with very poor quality ("E") in the inversion and

assigned them a null weight. In general, the quality could be linked to the signal-to-noise ratio (SNR), and that, because borehole data have a better SNR, they were systematically assigned an "A" quality. Also note that in order not to bias the distance to nodal planes by the larger number of borehole sensors with repetitive and consistent observations, they were considered only as a single station, the location of which corresponds to the mean of all borehole sensor locations. In practice, that means GM1, VW2, and PS3 counted as three stations in total in the inversion. Initial tests that we conducted without assigning weights showed that weights do not affect the solutions other than making them more stable and even more reliable.

Because a combination of borehole and surface sensors was used, we defined another quality factor Q_5 to rate the source mechanism solution. As the determination of first-arrival polarities on the borehole data was much less ambiguous than on the surface data (due to a higher SNR), we computed the percentage of polarity measurements made at the surface (i.e., an event in which polarity assignments were possible on all surface stations is considered as more reliable than an event in which only a few surface stations were included). We also took into account the quality assigned to each polarity and used the same weighting scheme as in the focal mechanism inversion ($w = 0.35$ for A, 0.3 for B, 0.25

$$\text{for C, } 0.1 \text{ for D, and } 0 \text{ for E}): Q_5 = \frac{\sum_i w_i}{\max(w) \times N_{\text{Surface stations}}},$$

in which w_i is the weight corresponding to the polarity measurement at

the i th surface station. To summarize, together with the definitions (Q_1 – Q_4) that we introduced in the previous section, we consider that one mechanism is better than another if (1) the number of polarity reversals is lower; (2) the number of potential solutions is smaller; (3) the azimuthal gap is smaller; and (4) the number of polarity measurements on the USGS and ISGS surface stations is higher. Taken separately, these assumptions are not always true, but their combination is. For example, obtaining a small number of potential solutions could either indicate a particularly well-constrained solution or, on the contrary, an overfitting solution. The number of measurements on the surface stations does not tell us anything about the distribution on the focal sphere, whether they are all concentrated in the same area or not. In our case, in general, whatever definition was used, good-quality events always scored the highest quality values and lower-quality events the smallest ones. That is why we finally considered a single-quality value by computing the mean of the five previously defined quality values for each mechanism and normalizing them to span the whole range of possible values (from 0% to 100%).

SENSITIVITY TESTS

The velocity model, as already mentioned, impacts directly the event location; the ray angles defining the station distribution over the focal sphere are, in turn, highly dependent on the velocity model as well.

We use a 1D velocity model, as shown in Figure 2. Up to 60 m above sea level (m.a.s.l.), velocities have been inferred by active seismic data (Will *et al.*, 2014). Above this level (i.e., from 60 m.a.s.l. to the surface), we used a combination of P -wave velocity logs made by the USGS (in shallow boreholes) and P - and S -wave velocity logs from the ISGS (within four boreholes; Bauer *et al.*, 2019). This model takes into account very low velocities measured in the surface glacial sediments and mainly improved the event location by reducing the time residuals for both P - and S -wave onsets at the surface stations.

Because we use a 1D velocity model, lateral variations in event location should not have a strong effect on ray angles, and we expect changes in event depth to be of greater influence. We here perform sensitivity tests by varying the depth of the northern cluster centroid. This is important because (1) depth determination is generally the weakest (or least) constrained part of event location, and (2) the 1D velocity model exhibits a sharp velocity contrast (from slower to faster velocities) at the inferred event depth. In Figure 4, we illustrate the influence of two different event depths (150 m difference) on the ray paths. When the event is located deeper (Fig. 4b,d), in the Precambrian basement, we observe that rays depart relatively horizontally for farther stations and more vertically for closer stations. This results in stations being distributed more toward the equator of the focal sphere, that is, at the rim of the polar projection. On the contrary, when the event is located shallower (Fig. 4a,c), in the Argenta formation, rays depart

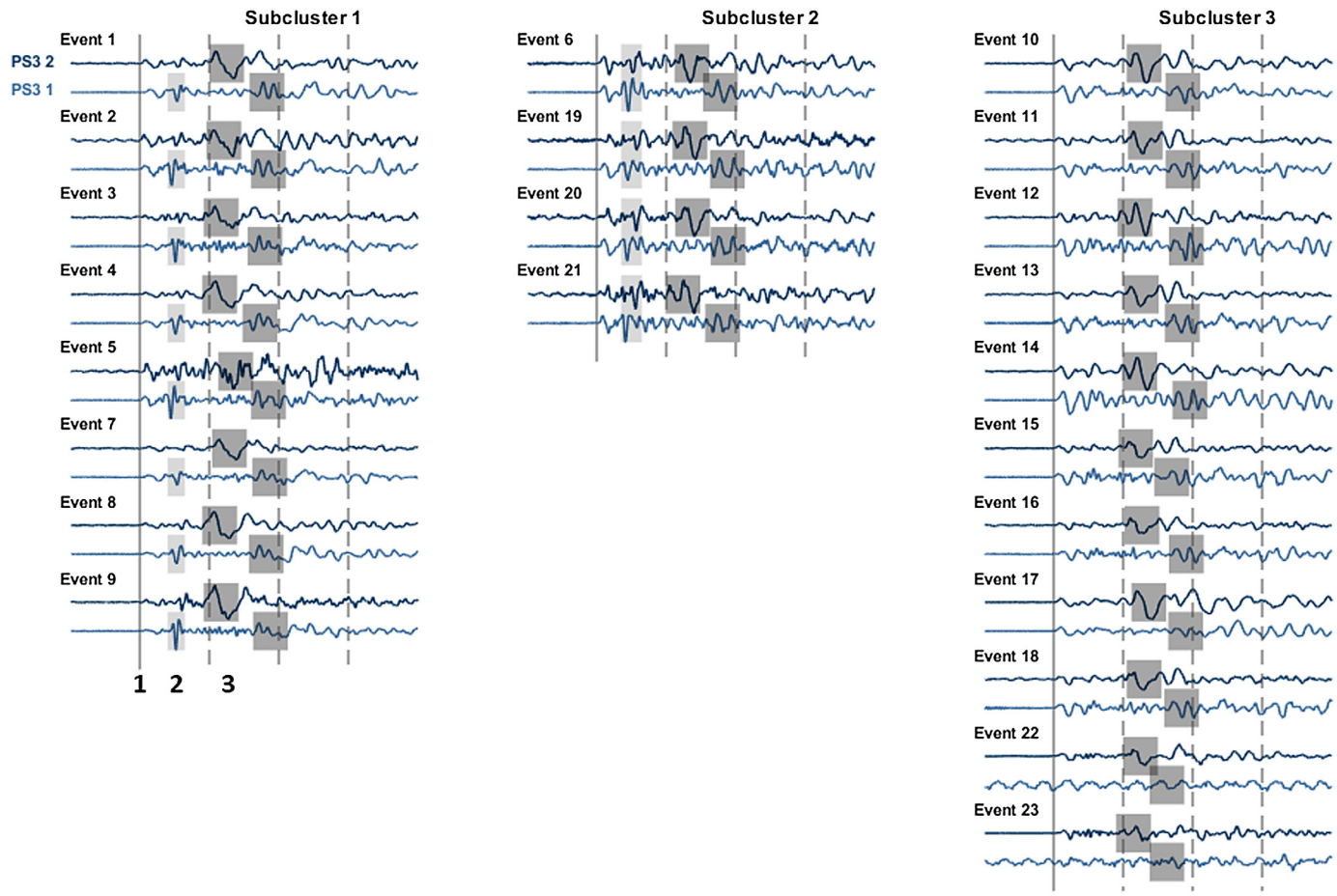
relatively vertically toward the stations, except for the two deep sensors PS3 1 and PS3 2. Stations are now being distributed more homogeneously on the focal sphere. Although the velocity model is quite detailed, the smallest layers are about 50 m width, and we expect the signal energy to be able to keep being transmitted to reach all stations.

Interestingly, headwaves traveling faster than the direct waves are observed for the two deepest downhole sensors (PS3 1 and PS3 2) in Figure 4c. We also see in Figure 4c,d that the existence of headwaves depends on event depth: when the event is located deeper, there is no faster layer below, so there is no headwave. This emphasizes how crucial the event depth is in this setup, potentially playing a role in the generation of headwaves. We will discuss this in the Results section.

The microseismicity at Decatur is clearly distributed in spatial clusters (Fig. 1). Goertz-Allmann *et al.* (2017) also showed the existence of subclusters within two of the main clusters and provided evidence showing the migration of events from the reservoir into the basement for these two clusters. The 23 events analyzed here, all belong to the north cluster, and the cross correlation of their waveforms around the P -wave arrivals at the two deepest sensors (PS3 1 and PS3 2) shows a clear clustering into three subclusters. In Figure 6, the waveforms recorded on the vertical component of both sensors are represented and cut in a 250 ms window around the manually picked first arrivals. The complex phase arrivals can be explained by the 1D velocity model, because the events are located around a sharp velocity contrast between the reservoir and the basement, at approximately 2000 m depth. For subcluster 1, the waveforms are characterized (1) by a strong secondary phase arrival (lighter shaded area in Fig. 6), particularly seen at PS3 1 and arriving earlier at PS3 1 compared with PS3 2 (upward traveling); and (2) by a third arrival (darker shaded area in Fig. 6), particularly seen at PS3 2. This phase seems to be of lower frequency than at PS3 1, and, this time, it also arrives later at PS3 1 (downward traveling).

Subcluster 2 roughly presents the same characteristics as subcluster 1, except that the secondary phase arrival is somewhat stronger at PS3 2 and the third phase arrival is delayed by a few milliseconds with respect to the first arrival.

Finally, for subcluster 3, the secondary phase arrival is hardly visible, whereas the third phase arrival is similar to subcluster 1. These observations can be explained by the sharp velocity contrasts at depth and are supported by ray tracing (Fig. 4c,d). The first arrival corresponds to a diving headwave, traveling faster in the basement (Fig. 4c, dashed lines). This agrees with our observation that it arrives first at the deepest sensor PS3 1 and then at PS3 2, whereas the third phase arrival corresponds to an upgoing wave traveling in a fast layer around 1400 m depth (Fig. 4c), arriving first at PS3 2 and then at PS3 1. These observed waveform characteristics and interpretations are in good agreement with the finite-difference full-waveform modeling performed by Goertz-Allmann *et al.* (2018). Hence,



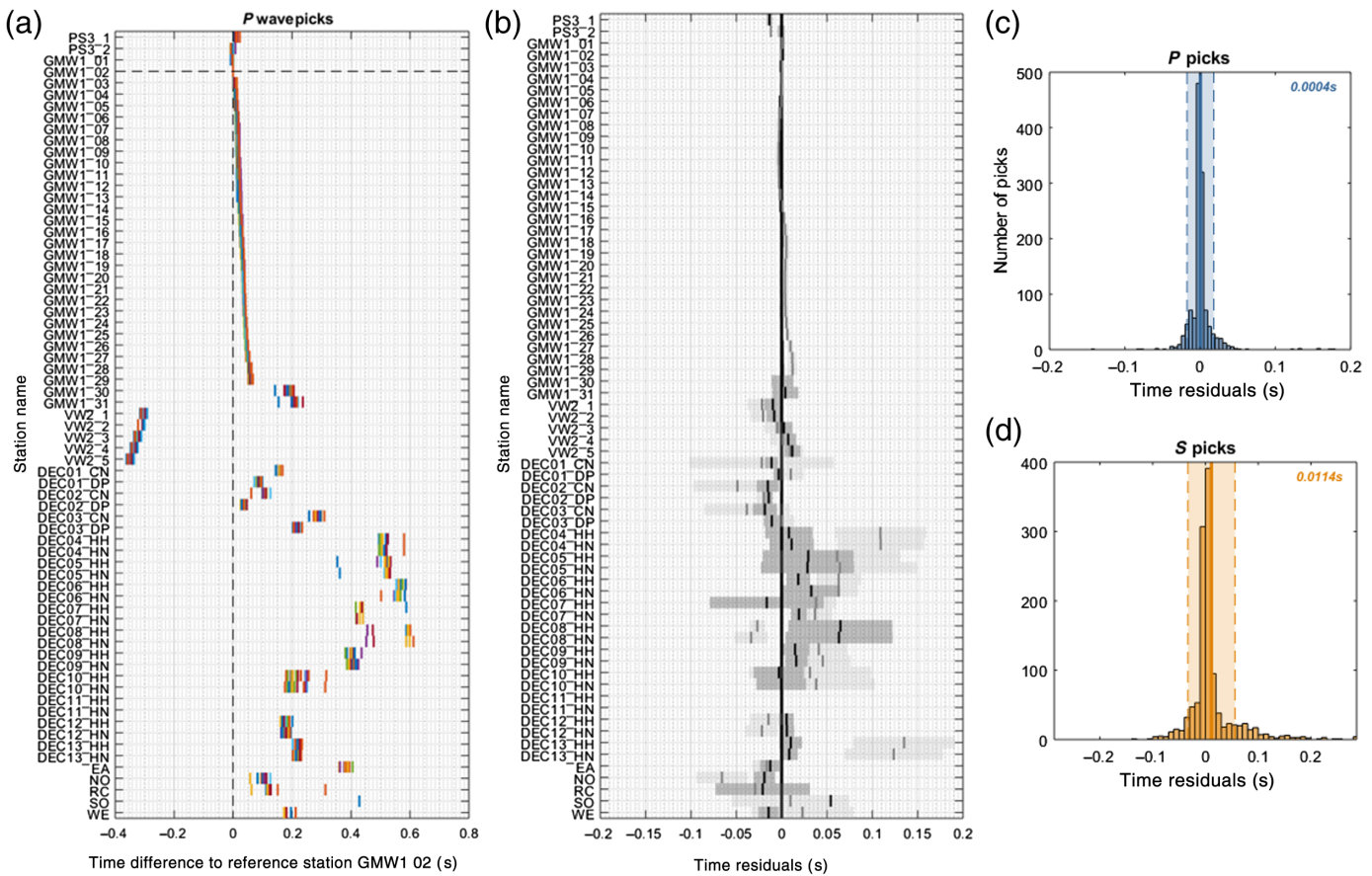
all the events are expected to be located above the basement. The slight difference observed in the third phase arrival times for events from subclusters 1 and 2 (later for 2) also suggests that events of subcluster 1 are located slightly shallower than events of subcluster 2.

EVENT LOCATION

Event location, and particularly event depth, is a critical factor for source mechanism determination, as we have just shown. The original catalog event locations were obtained using an anisotropic 1D velocity model and are based solely on the downhole recordings (PS3, GM1, and VW2). The anisotropy was calibrated using check shots farther away from the analyzed cluster and affected only a given layer. Therefore, we decided not to consider anisotropy and rather took advantage of the additional surface data. Integrating the USGS and ISGS surface data can greatly improve the azimuthal coverage and allows for better constrained event locations. For that reason, we relocated the events and used the new locations for further analysis. We have already shown in Figure 6 that the waveforms are quite complex at the deepest sensors with different phase arrivals. Therefore, the resulting locations strongly depend on which phase arrivals are included in the inversion. We picked the first arrival as the (*P*) headwave and the third arrival as the direct *P* wave.

Figure 6. Waveforms recorded on the vertical component of the two down-hole sensors PS3 1 and PS3 2 for the three subclusters. PS3 1 is the deepest sensor and corresponds to the second waveform plotted in each pair. The 250 ms waveforms are aligned on their first arrivals (continuous vertical line). Vertical dashed lines are set every 50 ms. Shaded areas correspond to the different arrivals visible (see the [Sensitivity Tests](#) section for more details). The color version of this figure is available only in the electronic edition.

Event location was performed in a two-step process with the goal of minimizing the root mean square of the residuals between observed and predicted arrival times: (1) one coarse 3D grid search, with a 200 m horizontal spacing and 50 m vertical spacing, which includes the whole area covered by the seismic network, followed (2) by a genetic algorithm (differential evolution [DE]) using an initial grid with reduced extension $600 \times 600 \times 100$ m centered on the previous location and with a finer resolution of 10 m in horizontal direction and 5 m in vertical direction. The main advantage of the DE method is that the final location is not restricted by the choice of the initial grid and converges faster toward the best location. We also chose to include those arrival times in the inversion that correspond to clear phase picks, and hence we considered only direct *P*-, head *P*-, and head *S*-wave arrival times for the PS3 deep sensors; the back azimuth measured around the *P* wave for the PS3 sensors (as the orientation of these sensors



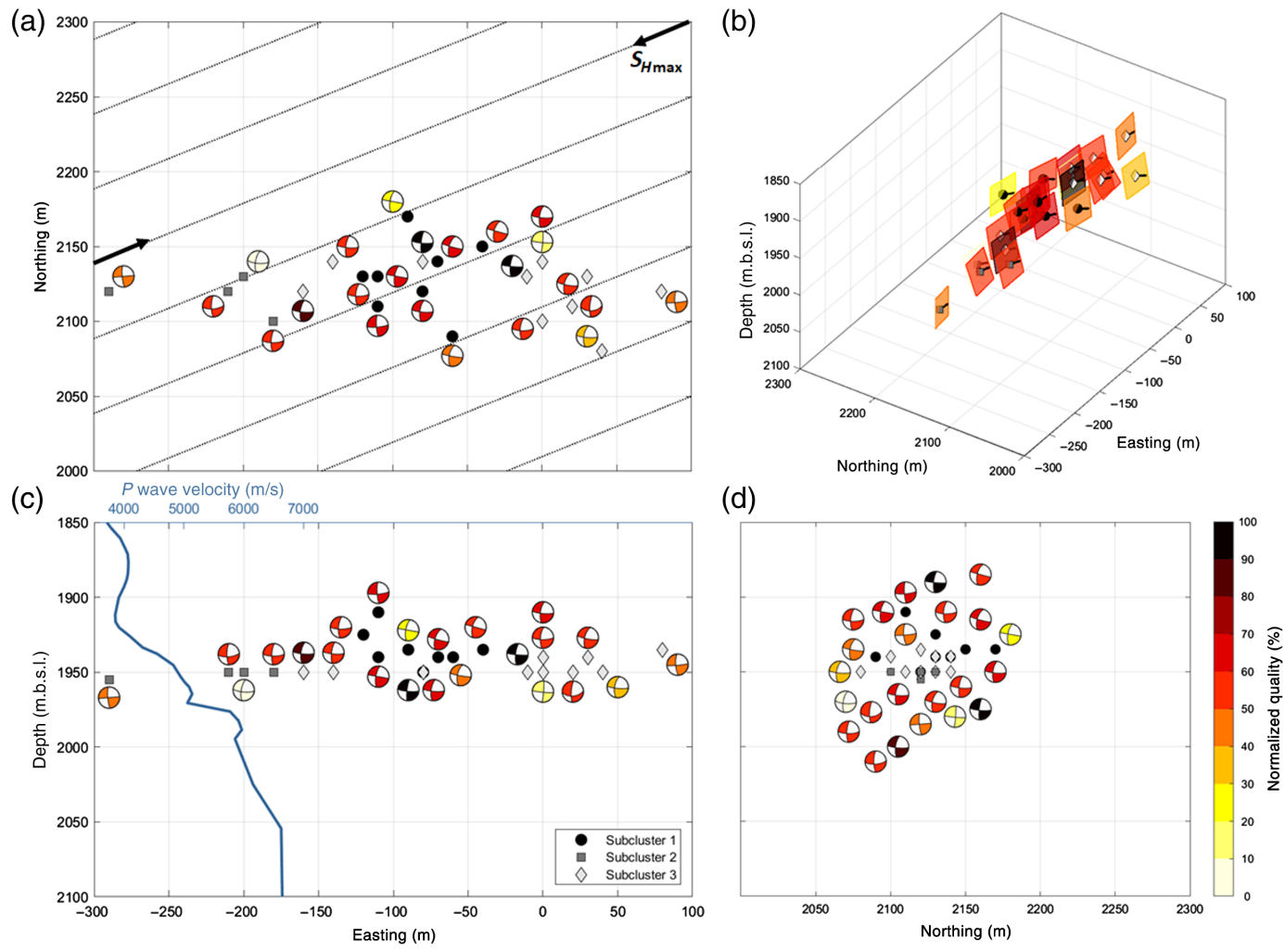
is known); the direct P -wave and S -wave arrival times for the GM1 and VW2 sensors, and the direct P -wave arrival times at all surface sensors. Weights are also applied in the minimization function and are inversely proportional to the picking errors that are assumed at each station.

The determination of the picking error values is databased and takes full advantage of the high-waveform similarity of events belonging to this cluster. In Figure 7a, station GM1_02 is taken as reference because all events were picked at this station, and picks at other stations are plotted as a function of their time difference to this reference. Because the waveforms are similar, this kind of plot could reveal whether some picks are obviously wrong (if they are too far off the others, then going back to the waveform data for checking), and we consider their spreading to reflect both the fact that the picks are slightly different because the event locations are different and the fact that the pick accuracy is not perfect. In other words, a small spread of picks indicates a good agreement and consistency for all events; a larger spread indicates lower agreement and more uncertainty. The standard deviations of the aligned picks at each station give the pick error values. Smaller pick errors are obtained for the borehole sensors (GM1, PS3, and VW2) with estimates in the order of 10 ms for P waves and 25, 50, and 100 ms for S waves, followed by the USGS and ISGS surface stations (variable from one station to another, but ranging from 30 to 150 ms for P and 100 to 200 ms for S). Higher uncertainties on S picks are usually

Figure 7. (a) Consistency and uncertainty in the direct P wavepicks (one color per event), taking one of the borehole sensors (GM1_02) as reference. This was used to assess pick errors in the weighting scheme for the root mean square minimization during the location inversion. (b) Mean and standard deviation of time residuals for P and S wavepicks (dark and light gray shades, respectively) after having located the events. (c) Distribution of time residuals for the P wave. (d) Distribution of time residuals for the S wave. The color version of this figure is available only in the electronic edition.

observed since the S -wave arrivals travel slower and are hidden in the P -wave coda in addition to being more spread over time. Higher uncertainties on VW2 S waves are due to difficulties in discriminating between direct S waves, S headwaves, and other incoming phases. Higher uncertainties at shallower stations are also expected because noise coming from external sources is more likely to affect the data and signals are much more attenuated. All in all, the resulting weighting scheme applied in the minimization function gives more confidence in the borehole observations than in the surface stations, but combining both is still important for obtaining the azimuthal coverage.

Locations of all 23 events are shown in Figure 8. We find that they are consistent with observations by Goertz-Allmann *et al.* (2017): the groups of similar events identified by cross correlation of waveforms are clustered nicely in space (Fig. 8), and the waveforms present different characteristics depending on whether the event is located slightly shallower or deeper.



Our tests reveal the importance of knowing the velocities in the subsurface and that, depending on the models, the residuals at the locations might increase or decrease. We obtain our best results for the velocity model shown in Figure 2, but the uncertainty in the P and S wavepicks and the time residuals plotted in Figure 7b still suggests that there are lateral and local variations of velocities within the first hundreds of meters below the surface that are not taken into account by the 1D velocity model, but could be incorporated in station corrections. Indeed, the largest residuals are still observed at the surface stations. Negative residuals correspond to overestimated velocities, whereas positive residuals correspond to underestimated velocities. The distribution of the time residuals both on P and S waves is Gaussian (see Fig. 7c,d). We also find that the location uncertainties are smaller in depth (a few tens of meters) than in horizontal directions (a few hundreds of meters). Details on how uncertainties were estimated are given in the supplemental material, as well as a comparison with the previous locations.

EVENT SOURCE MECHANISMS

A primary motivation of this work was to combine observations at all available stations to get better constraints on source

Figure 8. Compilation of source mechanisms for the 23 events of the north cluster. Each gray symbol (dot, square, and diamond) represents a seismic event belonging to one of the three subclusters. The focal mechanism plots are colored by their quality level computed with various criteria (see the [Prerequisites and Practical Approach for Determining Source Mechanisms](#) section for more details) and viewed from top, projected onto the lower hemisphere (note that focal mechanism plots are not rotated on vertical sections). The warmer the color, the better the mechanism. (a) Map view superimposed with the maximum principal stress $S_{H\max}$. (b) 3D view of the fault planes. Black arrows are slip vectors. (c) EW–depth section superimposed with the P -wave velocity model. (d) NS–depth section. The color version of this figure is available only in the electronic edition.

mechanisms. An example is given in Figure 9 for one of the events for which a satisfying, but nonoptimum, number of polarity measurements could be obtained from the surface stations.

The example in Figure 9 is particularly instructive and representative of the value of combining both borehole and surface stations. First, in Figure 9a, in which only borehole observations (PS3, GM1, and VW2) were used for the inversion, the wide range of potential solutions (about 2000) tells us how badly constrained the inversion is and that, therefore, the “best” solution may not be trusted. This is the result of

insufficient coverage over the focal sphere; all observations are concentrated on two lines in the southeast quadrant of the sphere, allowing almost any mechanisms to suit the data. Second, in Figure 9b, only surface station observations were used for the inversion. It is clear that the azimuthal station coverage of the focal sphere is much better. This results in a reduced number of potential solutions (1000) with zero polarity reversal, discarding some mechanisms, but still allowing for a large variety of them. In this example, it is also interesting to note that the number of solutions increases when allowing for one or two reversals, indicating that the best solution is highly unstable and cannot be trusted here either. Finally, Figure 9c displays the result of the inversion for the combination of all available observations. The number of potential solutions drops to only eight: they appear to be quite similar to each other, only varying by a few degrees, and exhibiting the same overall strike-slip mechanism. In that specific example, even the solutions with one reversal return a similar mechanism. Out of the 23 events, we have several examples in which the surface measurements appear to be self-sufficient. In these cases, although the borehole measurements are not complementary, they are supplementary and in total agreement with the surface observations, therefore providing a lot more confidence in the solution.

All following mechanisms shown in the article are the result of the inversion of both surface and borehole observations. We thoroughly processed each selected event and present the results in Figures 8 and 10 and Table 1. Each focal mechanism plot represents the stereographic projection of the lower hemisphere of the focal sphere (in compliance with the usual convention) and that the disambiguation between fault and auxiliary planes was based on the maximum stress-field direction (see the [Discussion](#) section). The color code corresponds to a quality factor, which was assigned to each event as described earlier in the article. Those quality factors reflect in a way the uncertainty on each individual mechanism. The last two columns of Table 1 also give the mean and standard deviation of the minimum rotation angles of all possible solutions with a minimum number of wrong polarities for each event with respect to the preferred solution, following the [Kagan \(1991\)](#) methodology. In principle, the smaller the rotation angle, the smaller the uncertainty. A general outcome from Table 1 is that the events with a larger number of surface observations (e.g., 17, 10, 14, ...) are also those with a smaller number of potential solutions that only slightly deviate from each other (which makes sense because the better azimuthal coverage does not allow whichever mechanisms to fit the data). To make the reader more easily aware that the highest mean quality values are associated with the highest individual quality factors, we present in the supplemental material the same results sorted by increasing quality values as well as the full range of potential fault solutions for each event (Table S3 and Fig. S4).

DISCUSSION

The resulting source mechanisms are predominantly strike slip and overall are very similar (Fig. 8), with an east–west striking and almost subvertical-dipping fault with slip direction around $-20^\circ/-10^\circ$. Only some slight variabilities in mechanisms are observed from one event to another. To identify more features common to all mechanisms, we project in Figure 11a the individual pressure and tension axes for each event and recall that the pressure axis is the one that bisects the dilatation (white) quadrants whereas the tension axis bisects the compressional (shaded) quadrants. We observe that the pressure axes are distributed relatively consistently within the northeast quadrant (40° – 60°) and with dips varying from 45° to 60° . These results are compatible within a 30° deviation limit around the maximum stress direction S_{Hmax} , which was determined in situ through various measurements (hydraulic fracturing and breakouts) and has an azimuth of N068° ([Bauer et al., 2016](#)) for being optimally oriented for strike-slip movements. In Figure 11b, the mechanisms are plotted on the triangular diagram introduced by [Frohlich \(1992\)](#). This graphical representation enables the mechanisms to easily be sorted into three main types of faulting, that is, normal, thrust, and strike slip, based on the dip angles of the pressure (P), tension (T), and null (B) axes. Almost all events have a nearly vertical null axis, therefore they are strike slip. Only one event falls into the “odd” category, that-is-to-say it does not belong firmly to any of the types of faulting but is close to strike slip.

We also compute a composite mechanism for the whole cluster, because the waveforms are very similar. In this respect, we take into account all polarity measurements available and keep the distribution on the focal sphere of each individual event (see Fig. 12a). The polarities are sometimes opposite to each other, in particular at DEC10 (top of the southwest quadrant) and DEC02 (close to the middle). At DEC02 (Fig. 13), we observed from time to time opposite polarities between the shallow sensor (Fig. 13a) and the deep sensor (Fig. 13b). The first sensor deployed at the surface is naturally mostly noisier, and we usually have greater confidence in the polarities measured on the buried sensor. Moreover, 150 m separates the sensors, and the waves travel through sediment deposits, so we cannot exclude the possibility that local heterogeneities could even reverse the polarities. However, despite the fact that the waveforms are similar, the first motion clearly appears to be positive for a few events (most visible for event 4 in Fig. 13b) and seems to account for the slight deviations that we see from one mechanism to another. Both DEC02 and DEC10 are stations close to the inferred fault plane.

As expected, the resulting composite mechanism is a strike-slip mechanism striking east–west (N095°), dipping 80° with a slip direction on the fault plane of -15° (left lateral, see Fig. 12b).

Overall, the obtained individual mechanisms are similar for all analyzed 23 events. Small variations between mechanisms can be explained by differences in data quality and/or number

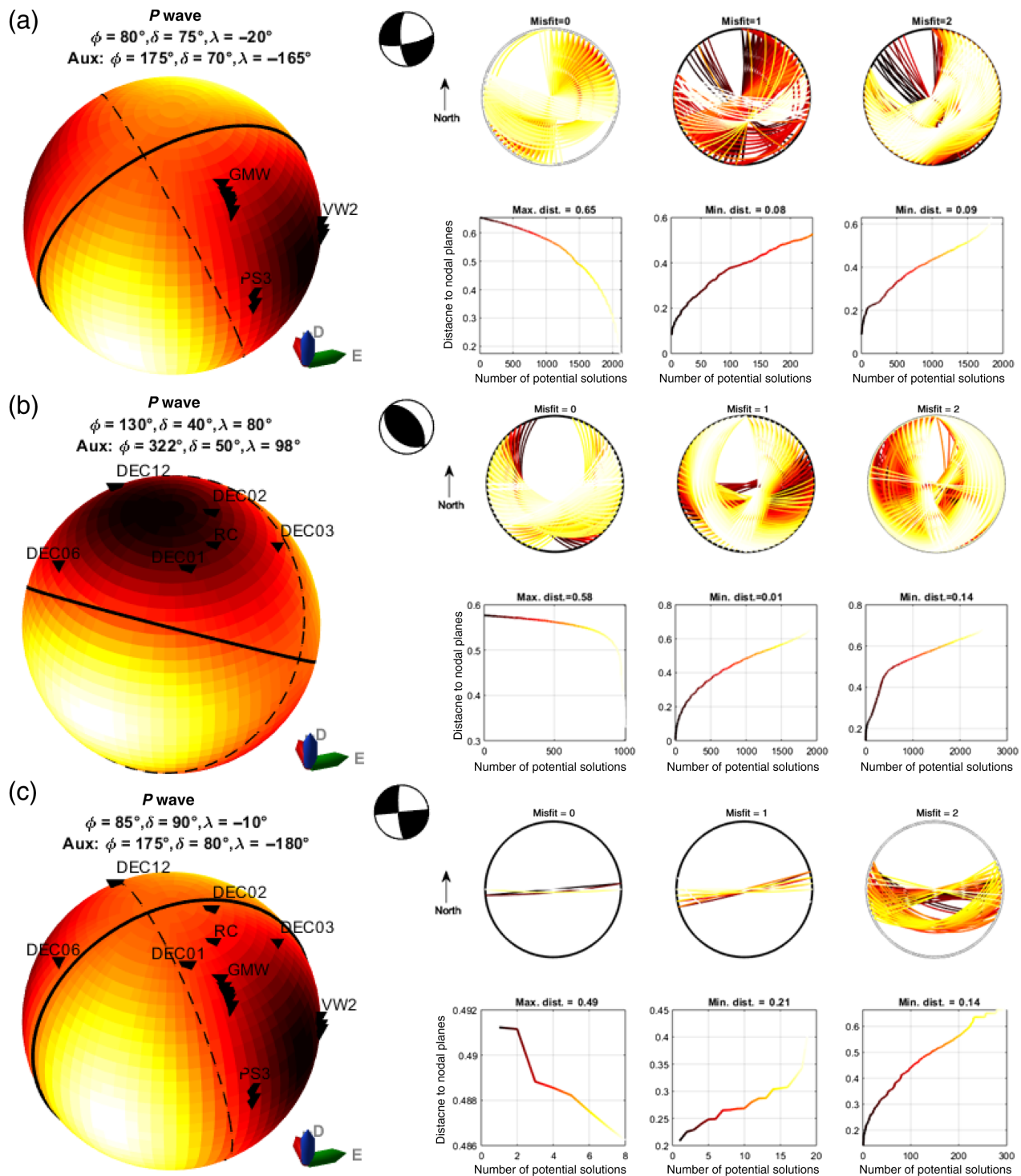


Figure 9. Comparison of the source mechanism best explaining the polarities for event 6 when using (a) only the borehole observations; (b) only the surface observations; and (c) both the borehole and surface observations. Each graph is composed of three plots. (1) The leftmost plots represent the focal sphere in 3D view (the north, east, and depth orientation is given in the right lowermost corner) colored by the *P*-wave radiation pattern coefficients for the best mechanism (going from light [negative] to dark [positive]). Reversed triangles symbolize the stations used in the inversion colored by their *P*-wave first-motion polarities (black for positive and white for negative), and the solid and dashed black lines correspond respectively to the fault plane and auxiliary plane (here, they remain arbitrary). (2) The

black-and-white focal mechanism plots in the middle are again the best solutions, as shown by the stereographic projection on the lower hemisphere of the focal sphere. (3) The rightmost plots show the range of potential fault planes for an increasing number of polarity reversals (from the minimum to up to two more reversals than the minimum). The associated curves below show the maximum (minimum, respectively) distance of the good measurements (reversals, respectively) to the nodal planes for each potential solution when the number of polarity reversals is zero (superior to zero, respectively). Each potential solution is colored from dark to light, respectively, for the best to the worst solutions. The color version of this figure is available only in the electronic edition.

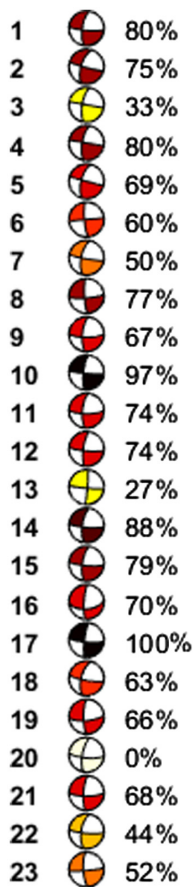


Figure 10. Lower hemisphere projection of the best mechanism for each event. The value in percent on the right gives the normalized quality and is obtained by combining differently some parameters of which values are given in Table 1. More details in the [Data Used and Practical Approach](#) section. The color version of this figure is available only in the electronic edition.

of measurements. The main mechanism is strike slip with the fault plane oriented east–west. This result is compatible with the general shape of the cluster in map view, which is elongated and seems to develop in an east–west direction, hence potentially revealing the existence of a fault aligned in that direction. The cluster is located at a considerable distance from the injection point (~2 km), beyond the extent of the CO₂ plume according to modeling results (fig. 6 in [Leetaru et al., 2014](#)). Together with the observation of pure-shear source mechanisms, this suggests that the observed microseismicity is likely not induced by the pressure front directly, but rather through stress changes in the area surrounding the reservoir.

Our resulting source mechanisms are also in agreement with the results obtained by [Kaven et al. \(2015\)](#) using the USGS surface data only. Six mechanisms are shown in figure 5 of their paper, of which two belong to the north cluster. One of them is a strike-slip mechanism very similar to ours. The other one is somewhat different but potentially fits with borehole observations that constantly show compressional (positive) first motion. The combination of borehole and surface measurements in our

analysis clearly allows us to get better constraints and confidence on the mechanisms. Similar mechanisms could very likely be assigned to all smaller events, which present similar waveforms on the borehole sensors but are hardly visible at the surface. This assumption can only be trusted because we have determined well-constrained focal mechanisms using the combined down-hole and surface networks.

No differences in mechanisms linked to the subclusters presented in Figure 6 are observed. The complexity of the waveforms is most probably due to local heterogeneities, and it is interesting to note that the individual events are located more or less within their subclusters: more westward for the events belonging to subcluster 2, shallower for the events belonging to subcluster 1, and more eastward for those belonging to subcluster 3. A recent study from [Freiburg et al. \(2019\)](#) has shown through petrophysical analysis, geophysical logs, and drill cores of the Precambrian basement at four wells CCS1, CCS2, VW1, and VW2 that the basement beneath the Illinois basin is compositionally and structurally heterogeneous. Interestingly, the VW2 well (the closest to the cluster) is located above a small area of anomalous reflectivity, and, this anomaly is interpreted to be caused by magnetite-rich gabbro rocks, occurring at depth of about 1969 and 1989 m at the well. This anomaly could explain the differences in the phases observed in the waveforms.

In the seismic volume, at depth between 1965 and 2080 m, [Freiburg et al. \(2019\)](#) also observed the presence of sets of parallel discontinuities that are striking east-northeast–west-southwest and north-northwest–south-southeast (fig. 8 of their paper). East-northeast-striking structures seem to consistently terminate on the north-northwest-striking structures, suggesting that they could represent earlier structures, and they appear to be mainly occurring to the west. However, east-northeast-striking discontinuities were not observed in the area of the cluster (which occur at the edge of the seismic cube). This might also be because vertical structures and, in particular, pure strike-slip faults with lack of vertical displacement are difficult to detect in seismic images.

During CO₂ injection, several processes may be involved in generating seismic events. [Villarrasa et al. \(2019\)](#) listed quite exhaustively mechanisms causing induced seismicity when storing CO₂. It turns out that, in general, it is the combination of several processes in close relation with the geology that favors the occurrence of seismic events in a given area for a given period.

Figure 14a displays the Mohr's circle for a given initial stress state. The effective stress values that we used are taken from the literature (more details given in the next paragraph) and correspond here to a strike-slip regime ($S_H > S_v > S_h$). The failure curve is plotted for a standard value of the friction coefficient ($\mu = 0.6$) and a cohesion of 8 MPa. The effective shear and normal stresses for any fault plane can be read on the Mohr circle through the angle β measured from $\sigma_{H\max}$ (N068°). The shaded area represents the range of strikes of the 23 analyzed events and shows that all fault planes are optimally oriented

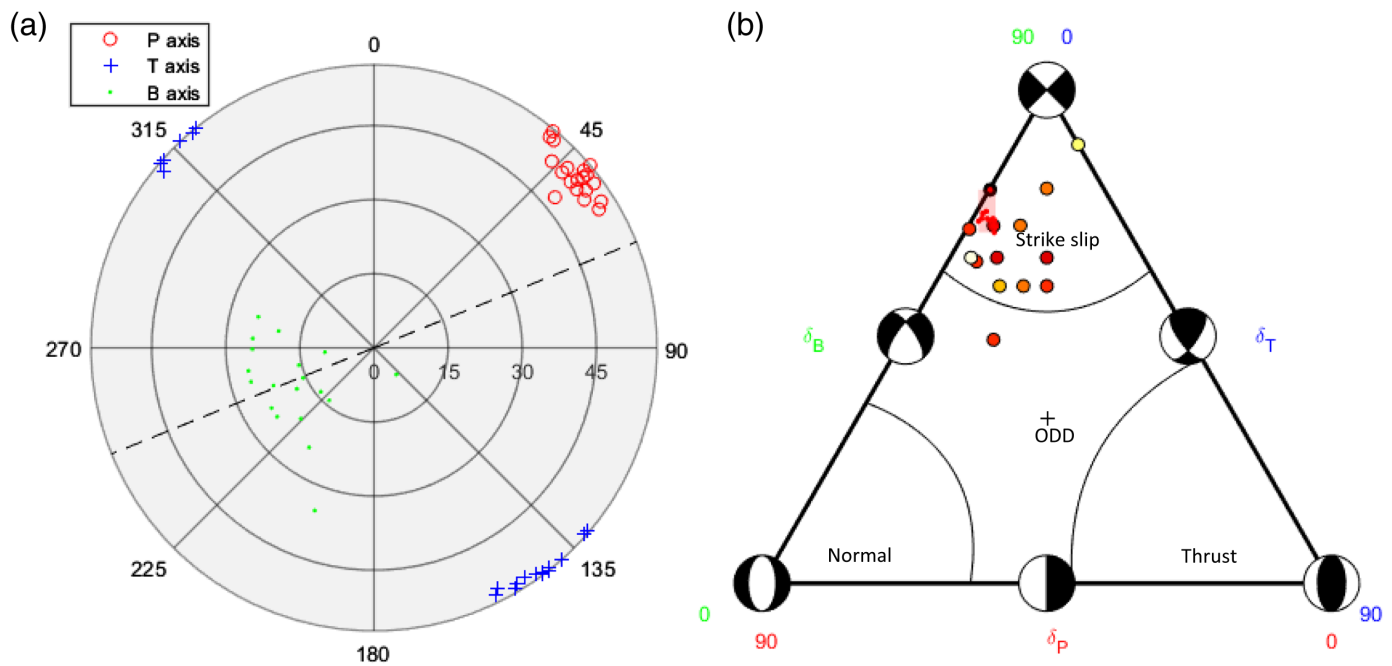


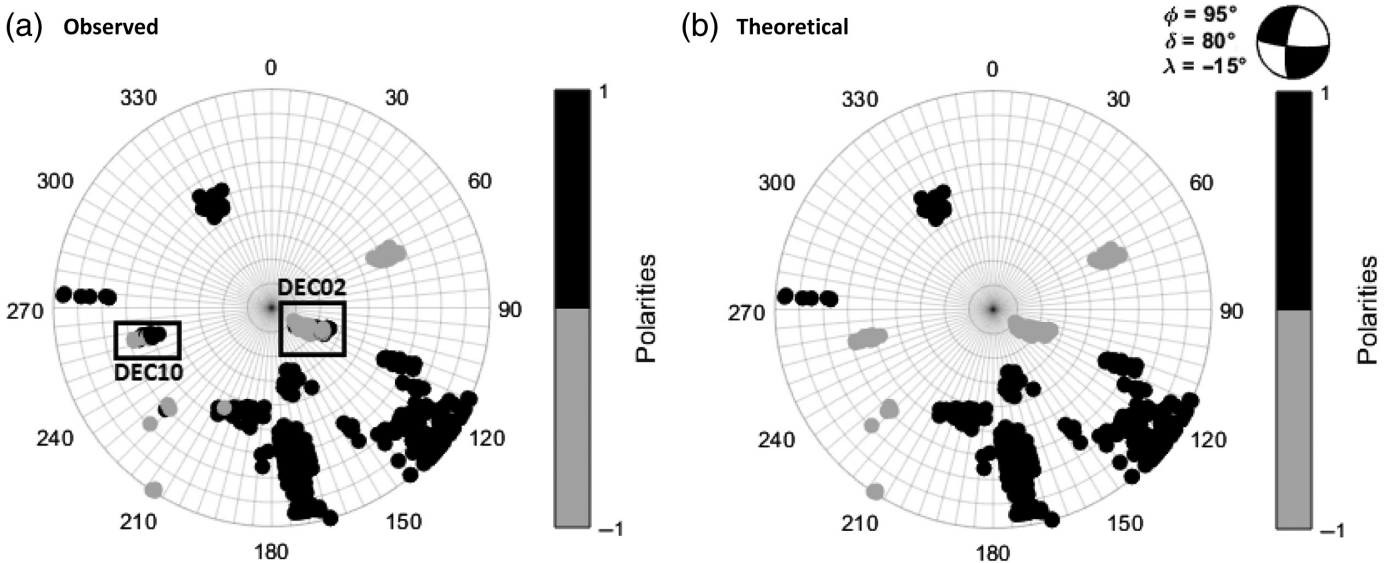
Figure 11. (a) Projection of the pressure (circles), tension (crosses), and null (dots) axes for every computed mechanism. The dashed line represents the direction of S_{Hmax} (N068°). (b) Triangle diagram following Frohlich (1992). Each dot represents a seismic event colored by its quality (see the Data Used

and Practical Approach section for details). The shaded area represents the composite focal mechanism. The color version of this figure is available only in the electronic edition.

TABLE 1
Results Summary

Event ID	Strike	Dip	Rake	Fault Type	Reversals (Numbers)	Solutions (Numbers)	Azimuthal Gap	Surface Observations (Numbers)	Mean Angle	Standard Angle
1	95°	80°	-20°	Strike slip	1	15	60°	10	12°	3°
2	105°	85°	-25°	Strike slip	0	1	90°	11	—	—
3	100°	90°	-20°	Strike slip	0	78	125°	7	70°	34°
4	100°	90°	-20°	Strike slip	0	13	65°	11	11°	4°
5	105°	90°	-25°	Strike slip	0	27	60°	7	17°	6°
6	85°	90°	-10°	Strike slip	0	8	100°	6	7°	2°
7	100°	85°	-25°	Strike slip	0	28	120°	7	17°	6°
8	85°	80°	-10°	Strike slip	1	9	60°	9	9°	3°
9	95°	75°	-20°	Strike slip	0	12	65°	8	10°	3°
10	95°	85°	-15°	Strike slip	1	3	60°	16	6°	1°
11	90°	75°	-20°	Strike slip	0	12	60°	8	9°	3°
12	95°	80°	-15°	Strike slip	0	8	60°	8	7°	2°
13	95°	85°	5°	Strike slip	1	92	105°	4	19°	7°
14	90°	80°	-20°	Strike slip	0	7	60°	13	10°	4°
15	95°	80°	-20°	Strike slip	0	3	60°	11	8°	4°
16	85°	55°	-15°	Odd	0	15	60°	7	11°	4°
17	95°	80°	-10°	Strike slip	0	2	60°	16	5°	0°
18	100°	80°	-25°	Strike slip	0	28	70°	7	22°	10°
19	85°	70°	-15°	Strike slip	0	18	65°	7	11°	3°
20	95°	75°	-20°	Strike slip	0	132	155°	3	31°	17°
21	90°	75°	-15°	Strike slip	0	12	65°	7	9°	3°
22	95°	80°	-25°	Strike slip	0	33	120°	5	13°	4°
23	85°	85°	-15°	Strike slip	1	65	60°	6	75°	29°

Each row of the table gives the best solution for each event as well as a certain number of parameters providing insight on their uncertainty and reliability: number of polarity reversals, that is, wrong polarities between predictions and observations; number of solutions minimizing the number of wrong polarities; azimuthal gap; number of surface observations; and mean and standard deviation of rotation angles of all potential solutions with respect to the best solution. Those angles were computed following Kagan (1991).



and close to failure. Figure 14a also illustrates the effect of a pore-pressure increase (ΔP): the effective stresses are reduced (the Mohr's circle moves to the left—dashed circle) and the failure conditions are met.

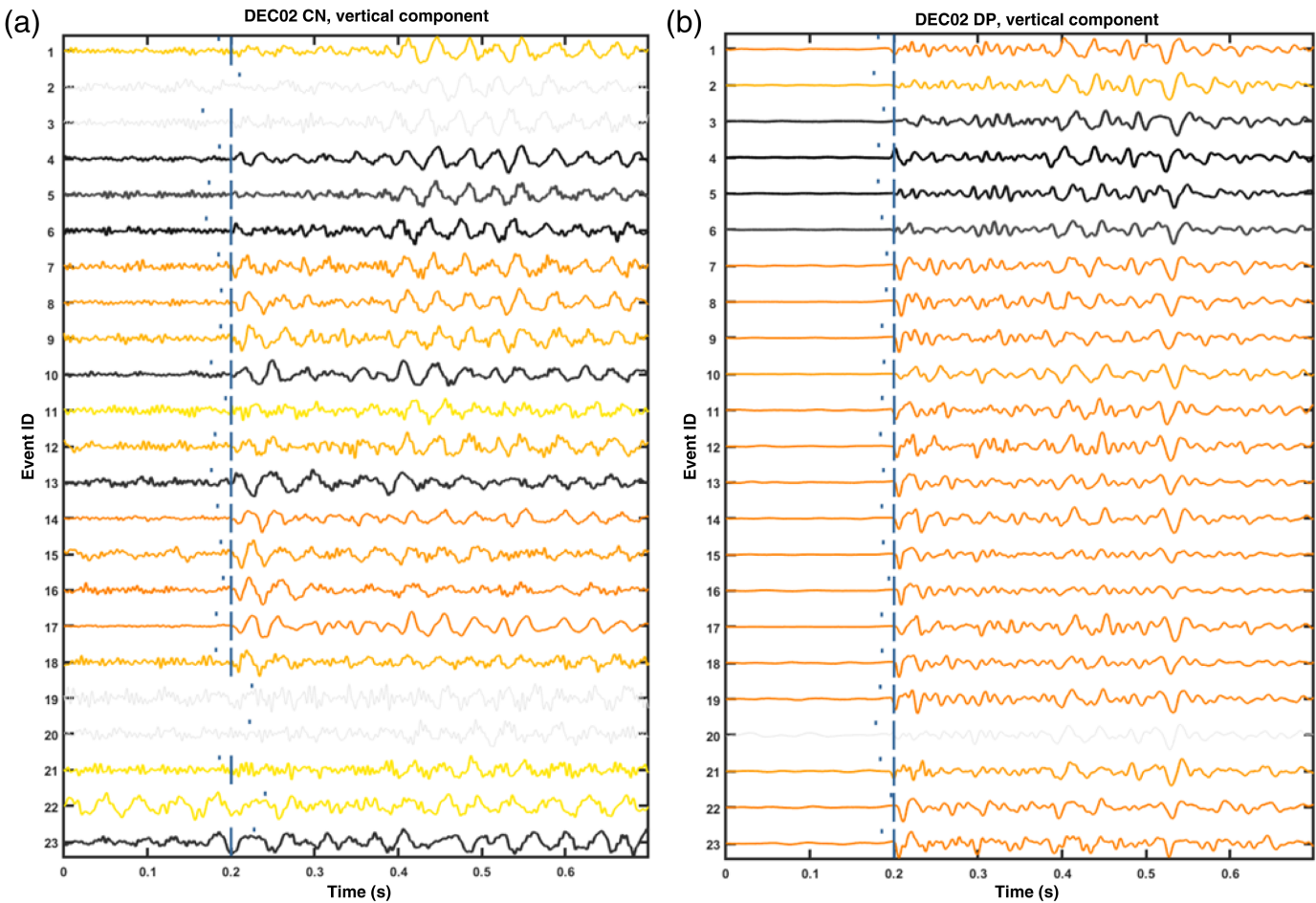
Figure 14b shows the reactivation potential (RP) of any faults depending on their orientation and was obtained following the same approach as Seithel *et al.* (2019). The approach consists of performing a Monte Carlo simulation for which the input parameters for each realization are randomly picked within their assumed uncertainty range (Gaussian distribution). The parameters to vary are the three principal stress magnitudes (S_H , S_h , S_v), the initial pore pressure (P_p), the friction coefficient μ , and the cohesion C . Because the stress magnitudes that we used were derived from stress gradients, we also made the event depth vary. The approach is interesting in the sense that it encompasses uncertainties on each parameter and allows to get an overview of which faults will preferably be activated under some given initial conditions and for the maximum expected pore-pressure increase ΔP_{max} .

The initial values and uncertainty ranges that we chose were taken and cross-checked both from published literature (Bauer *et al.*, 2016; Lahann *et al.*, 2017) and ISGS reports, and both for the IBDP site and at a larger scale (i.e., Illinois basin). In situ stress measurements are most often reported as gradients (MPa/km). Those are not true gradients from the surface downward, but gradients within layers of similar lithologic materials with similar properties at the same depth. The stiffer the materials, the higher the stress; the weaker the materials, the lower the stress. As a consequence, depending on rock formation, at an equivalent depth, the in situ measured stress can be very different. Such behavior had been observed at the IBDP site. Finally, we chose mean values of 22.8, 25, and 61.3 MPa/km with standard deviations of 4, 2, and 15 for S_h , S_v , and S_H , respectively. The values for S_h and S_v are very close to each other and may overlap, but are consistent with the stress regime for the Illinois

Figure 12. Polar projections showing (a) the concatenation of all polarity measurements for all events (dark, positive; light, negative), taken as input for the composite mechanism inversion; (b) the theoretical polarities corresponding to the best composite mechanism. The associated focal mechanism plot in stereographic projection is shown on the top right corner.

basin, which is most commonly strike slip with some reverse faulting (Lahann *et al.*, 2017). The mean pore-pressure value is 10.4 MPa/km with a standard deviation of 1.5. We took a mean event depth of 1950 m and assigned a 150 m standard deviation. The friction coefficient ranges from 0.5 to 0.7 and the cohesion from 0 to 12 MPa. The last parameter to set is the maximum expected pore-pressure increase. Bauer *et al.* (2016) reported a maximum increase of 1.14 MPa for one layer in a verification well located about 300 m from the injection well. The north cluster is located much farther (about 1500 m), hence a much smaller increase must be expected. However, we kept the value of 1.14 MPa as it may only affect the value of the RP (in %), and not the shape of the curve.

Unsurprisingly, Figure 14b shows that the potential for fault reactivation is higher when the faults deviate 30° from the maximum stress-field direction (Zang and Stephansson, 2010). Again, the shaded area shows the range of strikes for the 23 analyzed events, highlighting the fact that all reactivated fault planes are optimally oriented with respect to the N068° stress-field orientation. The vertical dotted lines correspond to the orientation of six other main clusters identifiable in Figure 1. Most of them seem to be optimally oriented as well, except one, and they may be activated by a larger pressure increase in comparison to the north cluster. In other words, that means the east–west-striking faults as observed in the north cluster could be reactivated by a smaller pressure increase. The modeling is crude: if we want to be more correct, we would also need to take into account the distance of events to the injection (i.e., we would not consider



a unique value of ΔP), and this would likely result in an RP curve showing peaks of different magnitudes. Moreover, as discussed earlier, the local geology and local conditions in close relation to the event location could affect the RP. For example, the topography of the layers at depth are not flat, which means that two events occurring at the same depth but at different lateral locations in the area could have different triggering criteria. All these considerations would require thorough geomechanical modeling (CO_2 plume and its pressure front) but is out of scope of this article. The approach used here is only valid for pure-shear failure and not for tensile failure. Future work should aim to compute focal mechanisms of events belonging to other clusters and determine whether and how the CO_2 injection could influence the activation and rupture criteria in those different clusters. In particular, it would be interesting to see whether the mechanisms involved are different at different clusters.

CONCLUSION

Microseismic monitoring via the installation of borehole sensors is often preferred over surface sensors because borehole data achieve a higher SNR, therefore improving the detectability of small-magnitude seismic events. Our study highlights the importance and usefulness of combining both, borehole and surface data, for further analysis, such as event location and

Figure 13. Waveforms recorded on the vertical component (oriented down) for all the events at (a) the surface station DEC02_CN and at (b) the collocated shallow borehole station DEC02_DP. The waveforms are colored in function of the polarity assigned (darker shades for positive and lighter shades for negative first-motion polarities, respectively). The shades are weaker when the confidence in the assigned polarity is decreasing. Very light-gray traces are those for which no polarity was assigned at all. The color version of this figure is available only in the electronic edition.

source mechanism determination. Borehole phase arrival picks and polarity measurements are more easily trusted, but their spatial extent is often limited. Surface data, on the contrary, present lower SNRs, in general, which limits the number of useable observations, but allows for a better spatial coverage. When both are combined, the results are better constrained and become more consistent.

Determining the causes of induced seismicity is far from being straightforward. Most often, not a single process but a combination of processes can account for the observations, and all observations are cross-related. Thus, the velocity model is crucial for event location, which, in turn, will influence the azimuthal coverage over the focal sphere. Conditions for event triggering will also be dependent on geology and initial stress conditions, which vary locally (both at depth and laterally).

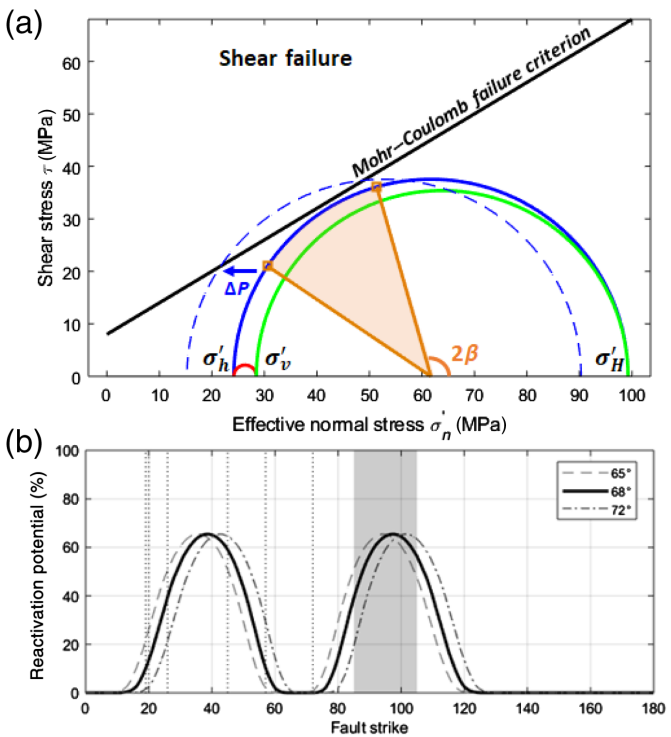


Figure 14. (a) Illustration of the effect of a pore-pressure increase on the Mohr's circle. (b) Fault reactivation potential as a function of the fault strike resulting from 10,000 Monte Carlo realizations. Detailed description given in the Discussion section. The color version of this figure is available only in the electronic edition.

We focused the analysis on 23 events located in the north cluster. The north cluster is located farther away from the injection point and has an east–west orientation, whereas most other clusters are oriented more northeast–southwest. We found that the event locations are consistent with the main resulting strike-slip mechanism, which is, in turn, consistent with the principal stress field. A relatively small increase in pore pressure could have the potential to trigger events on such east–west-oriented fault.

The shape and orientations of the other microseismic clusters also suggest slip on planes that are optimally oriented with respect to the principal stresses. In further work, a better understanding of the processes involved could be developed, such as pure-shear failure in response to pressure front propagation, associated tensile opening, and stress redistribution. The triggering of events in different clusters that indicate locations of existing faults reveals part of the structural complexity of the subsurface. However, faults that are not favorably oriented could also be present, yet they may not produce seismicity. Any directional fluid pressure migration would require hydraulic connection or stress transmission between roughly parallel microseismic event trends. Future work on geological strain scenarios that integrate the basin structural history with the seismic and microseismic data interpretations may provide

support for the existence of additional fluid pathways that connect the induced seismicity clusters.

DATA AND RESOURCES

Data are provided by the Midwest Geological Sequestration Consortium (MGSC). The Illinois Basin - Decatur project (IBDP) is a public–private partnership among government agencies, private companies, consultancies, and research organizations. Data used to generate the results presented here are provided as supporting information and are available upon request. The facilities of Incorporated Research Institutions for Seismology (IRIS) Data Services, and specifically the IRIS Data Management Center, were used for access to the U.S. Geological Survey (USGS) waveforms and related metadata used in this study. IRIS Data Services are funded through the Seismological Facilities for the Advancement of Geoscience and EarthScope (SAGE) Proposal of the National Science Foundation under Cooperative Agreement EAR-1261681. The codes for computing the source mechanisms have been developed by the authors and are now part of Norwegian Seismic Array's (NORSAR's) internal microseismic data analysis software that was also used for general data processing as well as ray paths computation. The focal mechanism plots in Figures 8 and 10 used a modified version of the focalmech function from [Conder \(2020\)](#). The plot in Figure 11b is based on an open-source code written by Miroslav Hallo (Prague, Czech Republic). The unpublished manuscript is from S. Williams-Stroud, R. A. Bauer, H. Leetaru, V. Oye, F. Stanek, S. E. Greenberg, and N. Langet, 2020, Induced seismicity hazard from potential fault reactivation by injection during the Illinois Basin - Decatur Project, *Bull. Seismol. Soc. Am.* The supplemental material provides a more exhaustive description of the seismic network, of the 23 events used in the study (timing, magnitude, location including uncertainties) as well as a table containing the 1D velocity model.

ACKNOWLEDGMENTS

The authors are grateful for support through the Climit program of Gassnova Project Number 618233. The Midwest Geological Sequestration Consortium is funded by the U.S. Department of Energy through the National Energy Technology Laboratory (NETL) via the Regional Carbon Sequestration Partnership Program (Contract Number DE-FC26-05NT42588) and by a cost share agreement with the Illinois Department of Commerce and Economic Opportunity, Office of Coal Development through the Illinois Clean Coal Institute. The authors thank A. Wüstefeld, Norwegian Seismic Array (NORSAR), leading the initiative on internal software development used for the analysis, and all the colleagues contributing. The authors also thank Jan Šílený from the Institute of Geophysics of the Czech Academy of Sciences and J. Ole Kaven from the U.S. Geological Survey (USGS) for their useful comments, which helped improve the article.

REFERENCES

- Albaric, J., V. Oye, N. Langet, M. Hasting, I. Lecomte, K. Iranpour, M. Messeiller, and P. Reid (2013). Monitoring of induced seismicity during the first geothermal reservoir stimulation at Paralana, Australia, *Geothermics* 52, 120–131.
- Bauer, R. A., M. Carney, and R. J. Finley (2016). Overview of microseismic response to injection into the Mt. Simon saline reservoir at the Illinois Basin-Decatur Project, *Int. J. Greenhouse Gas Control* 54, 378–388.

- Bauer, R. A., T. H. Larson, B. Curry, A. Anderson, and T. Young (2019). Vp-Vs measurements of glacial overburden: Illinois Basin-Decatur Project, Illinois State Geological Survey Report.
- Conder, J. (2020). focalmech(fm, centerX, centerY, diam, varargin), MATLAB Central File Exchange, available at <https://www.mathworks.com/matlabcentral/fileexchange/61227-focalmech-fm-centerx-centery-diam-varargin> (last accessed June 2020).
- Couëslan, M. L., R. Butsch, R. Will, and R. A. Locke (2014). Integrated reservoir monitoring at the Illinois Basin - Decatur Project, *Energy Procedia* **63**, 2836–2847.
- Finley, R. J., S. M. Frailey, H. E. Leetaru, O. Senel, M. L. Couëslan, and M. Scott (2013). Early operational experience at a One-million Tonne CCS demonstration project, Decatur, Illinois, USA, *Energy Procedia* **37**, 6149–6155.
- Freiburg, J. T., J. H. McBride, D. H. Malone, and H. E. Leetaru (2019). Petrology, geochronology, and geophysical characterization of Mesoproterozoic rocks in central Illinois, USA, *Geosci. Front.* **11**, 581–596.
- Freiburg, J. T., D. G. Morse, H. E. Leetaru, R. P. Hoss, and Q. Yan (2014). A depositional and diagenetic characterization of the Mt. Simon Sandstone at the Illinois Basin - Decatur Project Carbon Capture and Storage Site, Decatur, Illinois, USA Illinois Geological State Survey Circular 583.
- Frohlich, C. (1992). Triangle diagrams: Ternary graphs to display similarity and diversity of earthquake focal mechanisms, *Phys. Earth Planet. In.* **75**, nos. 1/3, 193–198.
- Furre, A.-K., O. Eiken, H. Alnes, J. Nesland Vevatne, and A.F. Kiær (2017). 20 years of monitoring CO₂-injection at Sleipner, *Energy Procedia* **114**, 3916–3926.
- Goertz-Allmann, B. P., S. J. Gibbons, V. Oye, R. A Bauer, and R. Will (2017). Characterization of induced seismicity patterns derived from internal structure in event clusters, *J. Geophys. Res.* **122**, no. 5, 3875–3894.
- Goertz-Allmann, B. P., D. Kühn, K. Iranpour, M. Jordan, B. U. Emmel, R. A. Bauer, V. Oye, and S. Greenberg (2018). Integrated active and passive seismic monitoring at the Decatur CCS project, Proc. of International Conf. on Greenhouse Gas Control Technologies (GHGT-14), Melbourne, Australia, 21–25 October 2018.
- Hardebeck, J. L., and P. M. Shearer (2002). A new method for determining first-motion focal mechanisms, *Bull. Seismol. Soc. Am.* **92**, no. 6, 2264–2276.
- Jost, M. L., and R. B. Herrmann (1989). A student's guide to and review of moment tensors, *Seismol. Res. Lett.* **60**, no. 2, 37–57.
- Julian, B. R., A. D. Miller, and G. R. Foulger (1998). Non-double-couple earthquakes 1. Theory, *Rev. Geophys.* **36**, no. 4, 525–549.
- Kagan, Y. Y. (1991). 3-D rotation of double-couple earthquake sources, *Geophys. J. Int.* **106**, 709–716.
- Kaven, J. O., S. H. Hickman, A. F. McGarr, and W. L. Ellsworth (2015). Surface monitoring of microseismicity at the Decatur, Illinois, sequestration demonstration site, *Seismol. Res. Lett.* **86**, no. 4, 1096–1101.
- Kwiatek, G. (2020). Radiation pattern from shear-tensile seismic source, MATLAB Central File Exchange, available at <https://www.mathworks.com/matlabcentral/fileexchange/43524-radiation-pattern-from-shear-tensile-seismic-source> (last accessed June 2020).
- Lahann, R. W., J. A. Rupp, C. R. Medina, G. Carlosn, and K. M. Johnson (2017). State of stress in the Illinois Basin and constraints on inducing failure, Missouri Department of Natural Resources, Missouri Geological Survey, Report of Investigations, Number 70, 282 pp.
- Lee, D. W., F. Mohamed, R. Will, R. Bauer, and D. Shelander (2014). Integrating mechanical earth models, surface seismic, and microseismic field observations at the Illinois Basin - Decatur Project, *Energy Procedia* **63**, 3347–3356.
- Leetaru, H. E., V. Smith, R. Will, J. Freiburg, and A. L. Brown (2014). The application of an integrated earth model in reservoir management of a plume, *Energy Procedia* **63**, 2903–2910.
- Mulvany, P. S., and T. L. Thompson. (2013). Paleozoic succession in Missouri, Part 1 (Revised) Cambrian System, Missouri Department of Natural Resources, Missouri Geological Survey, Report of Investigations, Number 70, 282 pp.
- Ou, G.-B. (2008). Seismological studies for tensile faults, *Terr. Atmos. Ocean. Sci.* **19**, no. 5, 463.
- Oye, V., E. Aker, T. M. Daley, D. Kühn, B. Bohloli, and V. Korneev (2013). Microseismic monitoring and interpretation with associated injection data from the In Salah storage site (Krechba), *Energy Procedia* **37**, 4191–4198.
- Rock, L., S. O'Brien, S. Tessarolo, J. Duer, V. Oropeza Bacci, B. Hirst, D. Randell, M. Helmy, J. Blackmore, C. Duong, et al. (2017). The Quest CCS project: Year review post start of injection, *Energy Procedia* **114**, 5320–5328.
- Seithel, R., E. Gaucher, B. Mueller, U. Steiner, and T. Kohl (2019). Probability of fault reactivation in the Bavarian Molasse Basin, *Geothermics* **82**, 81–90.
- van der Baan, M., D. Eaton, and M. Dusseault (2013). Microseismic monitoring developments in hydraulic fracture stimulation, in *Effective and Sustainable Hydraulic Fracturing*, Chapter 21, IntechOpen Editions, London, United Kingdom, 439–466, doi: [10.5772/56444](https://doi.org/10.5772/56444).
- Vilarrasa, V., J. Carrera, S. Olivella, J. Rutqvist, and L. Laloui (2019). Induced seismicity in geologic carbon storage, *Solid Earth* **10**, 871–892.
- Will, R., G. El-Kaseeh, P. Jaques, M. Carney, S. Greenberg, and R. Finley (2016). Microseismic data acquisition, processing, and event characterization at the Illinois Basin - Decatur Project, *Int. J. Greenhouse Gas Control* **54**, no. 1, 404–420.
- Will, R., V. Smith, D. Lee, and O. Senel (2016). Data integration, reservoir response, and application, *Int. J. Greenhouse Gas Control* **54**, no. 1, 389–403.
- Will, R., V. Smith, H. E. Leetaru, J. T. Freiburg, and D. W. Lee (2014). Microseismic monitoring, event occurrence, and the relationship to subsurface geology, *Energy Procedia* **63**, 4424–4436.
- Zang, A., and O. Stephansson (2010). *Stress Field of the Earth's Crust*, Chapter 5, Springer Editions, Dordrecht, The Netherlands, 89–100, doi: [10.1007/978-1-4020-8444-7](https://doi.org/10.1007/978-1-4020-8444-7).
- Zang, A., V. Oye, P. Jousset, N. Deichmann, R. Gritto, A. McGarr, E. Majer, and D. Bruhn (2014). Analysis of induced seismicity in geothermal reservoirs—An overview, *Geothermics* **52**, 6–21.

Manuscript received 17 February 2020

Published online 14 July 2020